Graduate School ETD Form 9
(Revised 01/14)

PURDUE UNIVERSITY
GRADUATE SCHOOL
Thesis/Dissertation Acceptance

This is to certify that the thesis/dissertation prepared

By Derek Douglas Scott

Entitled AN INVESTIGATION OF PARITY AND TIME-REVERSAL SYMMETRY BREAKING IN TIGHT-BINDING LATTICES

For the degree of Doctor of Philosophy

Is approved by the final examining committee:

Dr. Yogesh Joglekar

Dr. Gabor Csathy

Dr. Ricardo Decca

Dr. Vitaly Tarasov

Dr. Horia Petrache

To the best of my knowledge and as understood by the student in the *Thesis/Dissertation Agreement. Publication Delay, and Certification/Disclaimer (Graduate School Form 32)*, this thesis/dissertation adheres to the provisions of Purdue University's "Policy on Integrity in Research" and the use of copyrighted material.

Dr. Yogesh Joglekar

Approved by Major Professor(s): _____

_____

Approved by: Dr. Ricardo Decca 04/14/2014

Head of the Department Graduate Program Date

AN INVESTIGATION OF PARITY AND TIME-REVERSAL SYMMETRY BREAKING IN TIGHT-BINDING LATTICES

A Dissertation

Submitted to the Faculty

of

Purdue University

by

Derek Douglas Scott

In Partial Fulfillment of the

Requirements for the Degree

of

Doctor of Philosophy

May 2014

Purdue University

West Lafayette, Indiana

For my grandparents, Arnel L. Shaw, Mazell H. Shaw, Ross R. Scott, and Florence H. Scott.

ACKNOWLEDGMENTS

First and foremost I would like to thank my advisor, Dr. Yogesh Joglekar, for his many years of guidance and ostensibly inexhaustible supply of patience. He has consistently encouraged me to perform at my best (often when I wasnt sure what my best was). It has been a true privilege having Yogesh as my mentor.

I also owe a debt of gratitude to Dr. Ricardo Decca for the many times he has taken to answer questions and discuss random physics topics over the years. Dr. Horia Petrache has also been a constant source of inspiration. His PHYS 600 course on Mathematical Physics was by far the most insightful and most enjoyable of my graduate career.

I am also grateful to Dr. Vitaly Tarasov from the IUPUI Math Department and Dr. Gabor Csathy from the Purdue Department of Physics for taking the time to serve on my thesis committee. Their comments and suggestions have been very helpful throughout my research.

TABLE OF CONTENTS

Page

LIST OF FIGURES

ABSTRACT

Scott, Derek Douglas Ph.D., Purdue University, May 2014. An Investigation of Parity and Time-Reversal Symmetry Breaking in Tight-Binding Lattices. Major Professor: Yogesh N. Joglekar.

More than a decade ago, it was shown that non-Hermitian Hamiltonians with combined parity ($\mathcal{P}$) and time-reversal ($\mathcal{T}$) symmetry exhibit real eigenvalues over a range of parameters. Since then, the field of $\mathcal{PT}$ symmetry has seen rapid progress on both the theoretical and experimental fronts. These effective Hamiltonians are excellent candidates for describing open quantum systems with balanced gain and loss. Nature seems to be replete with examples of $\mathcal{PT}$-symmetric systems; in fact, recent experimental investigations have observed the effects of $\mathcal{PT}$ symmetry breaking in systems as diverse as coupled mechanical pendula, coupled optical waveguides, and coupled electrical circuits.

Recently, $\mathcal{PT}$-symmetric Hamiltonians for tight-binding lattice models have been extensively investigated. Lattice models, in general, have been widely used in physics due to their analytical and numerical tractability. Perhaps one of the best systems for experimentally observing the effects of $\mathcal{PT}$ symmetry breaking in a one-dimensional lattice with tunable hopping is an array of evanescently-coupled optical waveguides. The tunneling between adjacent waveguides is tuned by adjusting the width of the barrier between them, and the imaginary part of the local refractive index provides the loss or gain in the respective waveguide. Calculating the time evolution of a wave packet on a lattice is relatively straightforward in the tight-binding model, allowing us to make predictions about the behavior of light propagating down an array of $\mathcal{PT}$-symmetric waveguides.

In this thesis, I investigate the the strength of the $\mathcal{PT}$-symmetric phase (the region over which the eigenvalues are purely real) in lattices with a variety of $\mathcal{PT}$-symmetric potentials. In Chapter 1, I begin with a brief review of the postulates of quantum mechanics, followed by an outline of the fundamental principles of $\mathcal{PT}$-symmetric systems. Chapter 2 focuses on one-dimensional uniform lattices with a pair of $\mathcal{PT}$-symmetric impurities in the case of open boundary conditions. I find that the $\mathcal{PT}$ phase is algebraically fragile except in the case of closest impurities, where the $\mathcal{PT}$ phase remains nonzero. In Chapter 3, I examine the case of periodic boundary conditions in uniform lattices, finding that the $\mathcal{PT}$ phase is not only nonzero, but also independent of the impurity spacing on the lattice. In addition, I explore the time evolution of a single-particle wave packet initially localized at a site. I find that in the case of periodic boundary conditions, the wave packet undergoes a preferential clockwise or counterclockwise motion around the ring. This behavior is quantified by a discrete momentum operator which assumes a maximum value at the $\mathcal{PT}$-symmetry-breaking threshold.

In Chapter 4, I investigate nonuniform lattices where the parity-symmetric hopping between neighboring sites can be tuned. I find that the $\mathcal{PT}$ phase remains strong in the case of closest impurities and fragile elsewhere. Chapter 5 explores the effects of the competition between localized and extended $\mathcal{PT}$ potentials on a lattice. I show that when the short-range impurities are maximally separated on the lattice, the $\mathcal{PT}$ phase is strengthened by adding short-range loss in the broad-loss region. Consequently, I predict that a broken $\mathcal{PT}$ symmetry can be restored by increasing the strength of the short-range impurities. Lastly, Chapter 6 summarizes my salient results and discusses areas which can be further developed in future research.

1. INTRODUCTION

> The more important fundamental laws and facts of physical science have all been discovered, and these are now so firmly established that the possibility of their ever being supplanted in consequence of new discoveries is exceedingly remote . . . Our future discoveries must be looked for in the sixth place of decimals. –Albert A. Michelson, 1894.

The twentieth century undoubtedly belonged to the field of quantum mechanics. From the atomic bomb to the modern cellular telephone, there is hardly any facet of society that quantum mechanics has not had a hand in shaping. This is due to the fact that quantum theory has been remarkably successful in explaining experimental results, and predicting various non-trivial and counterintuitive phenomena. In contrast to the determinism of classical mechanics, quantum mechanics is a probabilistic theory in nature. We no longer speak of particles traveling on sharply-defined trajectories in space and time. Instead, we are relegated to assigning probabilities to specific outcomes. The axioms characterizing quantum mechanics are predominantly physical constraints, such as requiring a real energy spectrum, an energy spectrum that is bounded from below, and a unitary (probability conserving) time evolution. There exists another axiom, less transparent perhaps, which requires that physical observables correspond to Hermitian operators [1, 2]. An operator A is said to be Hermitian with respect to the standard inner product

$$\int \left(A^{\dagger}\psi\right)^{*} \psi dx = \int \psi^{*} A\psi dx, \tag{1.1}$$

when $A = A^{\dagger}$. This single axiom has significant implications regarding the energy spectrum and energy eigenvectors of the system.

Consider a Hamiltonian H and an energy eigenvector $|\psi_n\rangle$ (given in Dirac notation), such that $H|\psi_n\rangle = E_n|\psi_n\rangle$. By the condition of Hermiticity, it must follow that

$$\begin{aligned}(\langle\psi_n|H|\psi_n\rangle)^\dagger &= \langle\psi_n|H|\psi_n\rangle,\\ (E_n\langle n|n\rangle)^\dagger &= E_n\langle n|n\rangle,\\ E_n &= E_n^*.\end{aligned} \tag{1.2}$$

So Hermiticity guarantees real energy spectra. We can also make an important statement regarding the eigenvectors of the system. Consider the two eigenvalue equations $\langle\psi_m|H|\psi_n\rangle = E_n\langle\psi_m|\psi_n\rangle$ and $\langle\psi_n|H|\psi_m\rangle = E_m\langle\psi_n|\psi_m\rangle$. By subtracting the Hermitian adjoint of the second equation from the first, we arrive at the important condition

$$(E_n - E_m)\langle\psi_m|\psi_n\rangle = 0. \tag{1.3}$$

This implies that, provided the eigenvalues E_n and E_m are non-degenerate, the energy eigenvectors are orthogonal. In the case that E_n and E_m are degenerate, we can always construct orthogonal eigenvectors in the subspace spanned by the corresponding eigenvectors. Lastly, we recall that the time evolution operator in quantum mechanics for a time-independent Hamiltonian is given by $U(t) = \exp(-iHt/\hbar)$ [3], where $\hbar = h/2\pi$ is the scaled Planck constant. The Hermiticity of the Hamiltonian ensures a unitary time evolution $U(t)U^\dagger(t) = U^\dagger(t)U(t) = \exp(-iHt/\hbar)\exp(+iHt/\hbar) = 1$, and by extension, conservation of probability. So we see that the seemingly abstract Hermiticity requirement for the Hamiltonian guarantees that two of the fundamental axioms of quantum mechanics are satisfied.

More than a decade ago, Bender and coworkers showed that a class of continuum non-Hermitian Hamiltonians, possessing a combined parity ($\mathcal{P}$) and time-reversal ($\mathcal{T}$) symmetry (i.e. $\mathcal{PT}H\mathcal{PT} = H$), exhibits real energy spectra over a range of parameters [4, 5]. Since their discovery, $\mathcal{PT}$-symmetric Hamiltonians have been extensively explored [6–11]. Traditionally, the parameter space over which the spectrum of the Hamiltonian is real (so that its eigenfunctions are simultaneous eigenfunctions of the

combined $\mathcal{PT}$ operation) is called the region of unbroken symmetry. Broken $\mathcal{PT}$ symmetry occurs when the Hamiltonian H and $\mathcal{PT}$ no longer share simultaneous eigenfunctions, although $[H, \mathcal{PT}] = 0$ still holds; consequently, the eigenvalues may be complex in this region.

We now outline the principles of $\mathcal{PT}$-symmetric quantum mechanics. The parity operator $\mathcal{P}$, in both classical and quantum mechanics, is responsible for spatial inversion. It is often used to check for chirality, or handedness, of the system – a specific chirality will appear as its mirror image after space reflection. Since $\mathcal{P}$ is a linear operator, it must satisfy the condition

$$\mathcal{P}(a|\phi\rangle + b|\psi\rangle) = a\mathcal{P}|\phi\rangle + b\mathcal{P}|\psi\rangle. \tag{1.4}$$

The action of $\mathcal{P}$ will look different depending on the form of the Hamiltonian, but in the continuum case expressed in terms of position x and momentum p its action is given by $x \to -x$ and $p \to -p$. We note that in the preceding example, the action of $\mathcal{P}$ was a coordinate inversion about the origin $x = 0$. This is not strictly necessary; we can choose any reference point about which to consider spatial inversion (e.g. $H = p^2 + (x+1)^2 - 1$ is $\mathcal{P}$-symmetric about $x = -1$).

The time-reversal operator $\mathcal{T}$ is responsible for the reversal of motion. In classical mechanics, this would correspond to the reversal of a particle's trajectory. In the case of quantum mechanics, however, we must use more caution. Unlike parity, $\mathcal{T}$ is an antilinear operator satisfying

$$\mathcal{T}(a|\phi\rangle + b|\psi\rangle) = a^*\mathcal{T}|\phi\rangle + b^*\mathcal{T}|\psi\rangle. \tag{1.5}$$

The action of $\mathcal{T}$ on the quantum mechanical position and momentum operators x and p is $x \to x$ and $p \to -p$, but we must also include complex conjugation $\mathcal{T}i\mathcal{T} = -i$ due to the antilinearity condition. In addition to preserving the canonical commutation relation $[x, p] = i\hbar$, the antilinearity requirement for $\mathcal{T}$ is necessary on physical grounds. If $\mathcal{T}$ were a linear operator, it can be shown that $\mathcal{T}$ and the Hamiltonian H would then anticommute (i.e. $-H\mathcal{T} = \mathcal{T}H$) [3]. If we now consider an energy

eigenvector $|\psi_n\rangle$ with a corresponding energy eigenvalue E_n, we would have, because of the anticommutator

$$H\mathcal{T}|\psi_n\rangle = -\mathcal{T}H|\psi_n\rangle = (-E_n)\mathcal{T}|\psi_n\rangle. \tag{1.6}$$

This means that the time-reversed state $\mathcal{T}|\psi_n\rangle$ is an eigenvector of the Hamiltonian with energy eigenvalues $-E_n$. This would violate the fundamental axiom of quantum mechanics requiring a lower bound on the energy spectrum. Even in the case of a free particle, it is well known that the energy spectrum is always positive semidefinite since there is no state with lower energy than a particle at rest. Therefore, in order for time-reversal to be a physical symmetry, complex conjugation (and hence, antilinearity) must be required.

An arbitrary operator A is said to possess unbroken $\mathcal{PT}$ symmetry when $[A, \mathcal{PT}] = 0$ *and* it shares simultaneous eigenfunctions with the $\mathcal{PT}$ operator – the $\mathcal{PT}$ symmetry is broken otherwise. We now consider a non-Hermitian Hamiltonian H with unbroken $\mathcal{PT}$ symmetry. If $|\phi_n\rangle$ is an eigenvector of H ($H|\phi_n\rangle = E_n|\phi_n\rangle$), it must also be true that $\mathcal{PT}|\phi_n\rangle = \lambda|\phi_n\rangle$. Therefore, it follows that

$$\begin{aligned}
\mathcal{PT}(\mathcal{PT}|\phi_n\rangle) &= \mathcal{PT}(\lambda|\phi_n\rangle), \\
\mathcal{P}(\mathcal{TP})\mathcal{T}|\phi_n\rangle &= \lambda^*\mathcal{PT}|\phi_n\rangle, \\
\mathcal{P}(\mathcal{PT})\mathcal{T}|\phi_n\rangle &= \lambda^*(\lambda|\phi_n\rangle), \\
\mathcal{P}^2\mathcal{T}^2|\phi_n\rangle &= |\lambda|^2|\phi_n\rangle, \\
|\phi_n\rangle &= |\lambda|^2|\phi_n\rangle,
\end{aligned} \tag{1.7}$$

where we have used the fact that the individual $\mathcal{P}$ and $\mathcal{T}$ operators commute. Since the eigenvalue λ is a pure phase ($\lambda = e^{i\alpha}$), we can choose the phase angle α such that $\mathcal{PT}|\phi_n\rangle = |\phi_n\rangle$. It follows that

$$\begin{aligned} \mathcal{PT}(H|\phi_n\rangle) &= \mathcal{PT}(E_n|\phi_n\rangle), \\ H(\mathcal{PT}|\phi_n\rangle) &= E_n^*(\mathcal{PT}|\phi_n\rangle), \\ H|\phi_n\rangle &= E_n^*|\phi_n\rangle, \\ E_n|\phi_n\rangle &= E_n^*|\phi_n\rangle, \\ E_n &= E_n^*. \end{aligned} \tag{1.8}$$

We see that when H and $\mathcal{PT}$ share simultaneous eigenfunctions we are guaranteed real energy spectra. We remind the reader that the fact that $[H, \mathcal{PT}] = 0$ does not automatically imply H and $\mathcal{PT}$ share simultaneous eigenfunctions since $\mathcal{T}$ is an antilinear operator. This can be easily seen since

$$\begin{aligned} \mathcal{PT}(H|\phi_n\rangle) &= \mathcal{PT}(E_n|\phi_n\rangle), \\ H(\mathcal{PT}|\phi_n\rangle) &= E_n^*(\mathcal{PT}|\phi_n\rangle), \end{aligned} \tag{1.9}$$

and we do not know a priori that the energy eigenvalues are real $E_n = E_n^*$, thus we cannot draw the conclusion that $\mathcal{PT}|\phi_n\rangle \propto |\phi_n\rangle$. The question remains, then, when are the eigenvalues real? In general, one cannot tell by inspection alone what values of the parameters in the Hamiltonian will give real energy spectra – the parameter space must be investigated analytically or (more often) numerically.

To illustrate these ideas, consider a simple 2×2 non-Hermitian Hamiltonian,

$$H = \begin{pmatrix} i\gamma & -J \\ -J & -i\gamma \end{pmatrix}, \tag{1.10}$$

where $J, \gamma \in \mathbb{R}^+$. The Hamiltonian H is clearly non-Hermitian since $H^\dagger = H^* \neq H$. The energy eigenvalues are given by $E_\pm = \pm\sqrt{J^2 - \gamma^2}$ and are shown in Fig. 1.1. The top panel shows the real part of the two energy eigenvalues $E_\pm$ as a function of γ (given in units of J). When $\gamma < J$, the eigenvalues are purely real, and the

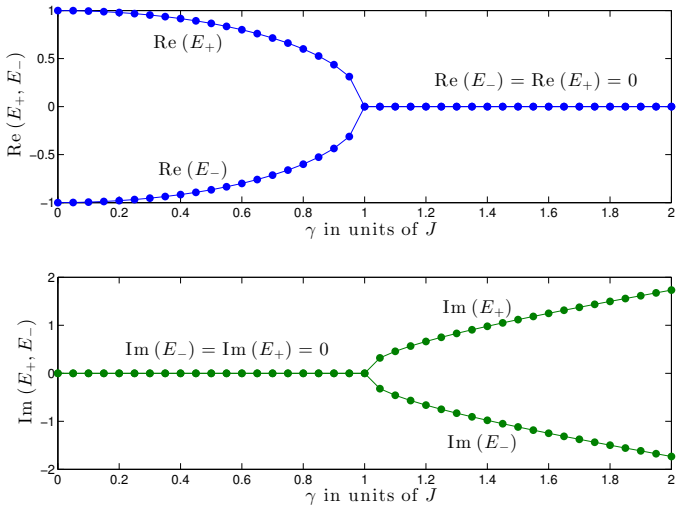

Fig. 1.1. Top Panel: Real part of the eigenvalues $E_\pm$ as a function of γ. For $\gamma < J$ the eigenvalues are purely real, hence the $\mathcal{PT}$ symmetry is unbroken. The real parts of the eigenvalues begin to converge, however, as γ increases towards J. At the $\mathcal{PT}$-symmetry-breaking threshold ($\gamma = J$), the eigenvalues become degenerate. Bottom Panel: For $\gamma > J$ the $\mathcal{PT}$ symmetry is broken, and the eigenvalues are purely imaginary.

$\mathcal{PT}$ symmetry is unbroken. As γ increases towards J, the two eigenvalues begin to converge until they become degenerate at the $\mathcal{PT}$-symmetry-breaking threshold $\gamma = J$. The bottom panel in Fig. 1.1 shows that for $\gamma > J$ the $\mathcal{PT}$ symmetry is broken, and the eigenvalues are purely imaginary.

To determine the corresponding eigenvectors of H, we must take into consideration whether we are in the region $\gamma \leq J$ or $\gamma > J$. In the case of $\gamma \leq J$, the normalized eigenvectors are given by

$$e_+ = \frac{1}{\sqrt{2}} \begin{pmatrix} \frac{J}{i\gamma - \sqrt{J^2-\gamma^2}} \\ 1 \end{pmatrix} \text{ and } e_- = \frac{1}{\sqrt{2}} \begin{pmatrix} \frac{J}{i\gamma + \sqrt{J^2-\gamma^2}} \\ 1 \end{pmatrix}. \tag{1.11}$$

When $\gamma = 0$, H is clearly Hermitian, and we recover the orthonormality property of the eigenvectors as expected. As gamma is increased through $\gamma \leq J$, the eigenvectors are no longer orthonormal, but they still remain linearly independent and, therefore,

span the relevant space. At the $\mathcal{PT}$-symmetry-breaking threshold $\gamma = J$, where the two energy eigenvalues $E_\pm$ converge, the eigenvectors are parallel, reflecting the degeneracy of the system. For $\gamma > J$, we must take caution when normalizing the eigenvectors and checking for orthonormality since the quantity $\sqrt{J^2-\gamma^2}$ is purely imaginary. The normalized eigenvectors in this case are given by

$$\begin{aligned} e_+ &= \left(\frac{2\gamma^2-J^2-2\gamma\sqrt{\gamma^2-J^2}}{2\gamma^2-2\gamma\sqrt{\gamma^2-J^2}}\right)^{1/2}\begin{pmatrix}\frac{J}{i\gamma-i\sqrt{\gamma^2-J^2}}\\ 1\end{pmatrix}, \\ e_- &= \left(\frac{2\gamma^2-J^2+2\gamma\sqrt{\gamma^2-J^2}}{2\gamma^2+2\gamma\sqrt{\gamma^2-J^2}}\right)^{1/2}\begin{pmatrix}\frac{J}{i\gamma+i\sqrt{\gamma^2-J^2}}\\ 1\end{pmatrix}. \end{aligned} \tag{1.12}$$

The inner product $e_+^\dagger \cdot e_- = J/\gamma$, indicating that, while not orthonormal, the eigenvectors are linearly independent. Fig. 1.2 shows what happens to the amplitude of the excited-state eigenvector over the transition from broken to unbroken $\mathcal{PT}$ symmetry. The top panel shows the eigenvector amplitude at the $\mathcal{PT}$-symmetry-breaking

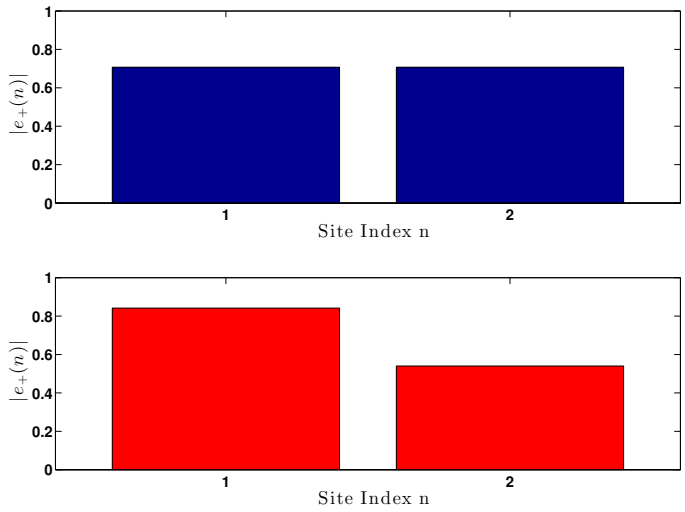

Fig. 1.2. Top Panel: Shows the amplitude $|e_+(n)|$ of the excited-state eigenvector for $\gamma = J$ at the $\mathcal{PT}$-symmetry-breaking threshold. The $\mathcal{PT}$ symmetry is still unbroken and hence the amplitude is symmetric in this region. Bottom Panel: For $\gamma = 1.1J$, the broken $\mathcal{PT}$ symmetry is manifest as an asymmetry in the eigenvector amplitude.

threshold $\gamma = J$, when the eigenvalues are still purely real. The unbroken $\mathcal{PT}$ symmetry is seen in the equal weights of the amplitude on the first and second index sites. In the bottom panel, the $\mathcal{PT}$ symmetry is broken since $\gamma = 1.1J$, and the resulting eigenvector amplitudes are now asymmetric. We also point out that the left eigenvectors of the Hamiltonian H are *not* equal to the adjoint of the right eigenvectors, as is the case for a Hermitian Hamiltonian. Broken $\mathcal{PT}$ symmetry also has dramatic consequences for the time evolution of a system. The presence of complex eigenvalues implies an exponential increase or decay (depending upon the sign) in intensity since the time-evolved state will involve terms with coefficients of the form $U(t) = \exp(-iE_n t/\hbar)$.

Lattice models, including tight-binding lattices, have been a cornerstone of theoretical explorations due to their analytical and numerical tractability [12]. In recent years, sophisticated optical-lattice systems have increasingly permitted the experimental exploration of lattice models [13, 14], although these models are largely based on Hermitian Hamiltonians. Recently, lattice models with non-Hermitian, $\mathcal{PT}$-symmetric Hamiltonians, and their experimental realizations in optical waveguides [15,16], large-scale temporal lattices [17], and coupled resistor-inductor-capacitor (RLC) circuits with balanced loss and gain [18], have become a focal point of research.

In this thesis, we investigate the $\mathcal{PT}$-symmetric phase in lattice models with both position-dependent and position-independent, parity-symmetric tunneling functions in the presence of $\mathcal{PT}$-symmetric impurities located at arbitrary ($\mathcal{P}$-symmetric) positions on the lattice. In addition, we explore the degrees and signatures of $\mathcal{PT}$ symmetry breaking in the time evolution of a single-particle wave packet initially localized at a site. The outline of this thesis is as follows. In Chapter 2, we review the features of the tight-binding lattice model in the absence of impurities, followed by an investigation of the $\mathcal{PT}$-symmetric phase in a one-dimensional lattice with uniform tunneling and two on-site $\mathcal{PT}$ potentials for open boundary conditions. Chapter 3 considers uniform $\mathcal{PT}$-symmetric rings, where we explore the time evolution of a wave packet initially localized to a single site of the lattice. We also study the development

of chiral motion in a wave packet across the $\mathcal{PT}$ phase boundary, and quantify this behavior by a discrete momentum operator. In Chapter 4, we investigate nonuniform lattices where the parity-symmetric hopping between neighboring sites can be tuned. We find that the $\mathcal{PT}$ phase remains strong in the case of closest impurities and fragile elsewhere. Chapter 5 explores the effects of competition between localized and extended $\mathcal{PT}$ potentials on a lattice. We show that when the short-range impurities are maximally separated on the lattice, the $\mathcal{PT}$ phase is strengthened by adding short-range loss in the broad-loss region. Consequently, we predict that a broken $\mathcal{PT}$ symmetry can be restored by increasing the strength of the short-range impurities. Lastly, Chapter 6 summarizes our salient results and discusses areas which can be further developed in future research.

2. ROBUST AND FRAGILE $\mathcal{PT}$-SYMMETRIC PHASES IN UNIFORM LATTICES

Evanescently-coupled optical waveguides [19] have provided a unique realization of a one-dimensional lattice with tunable tunneling amplitudes [20], disorder [21], and non-Hermitian, on-site, impurity potentials [22]. The evanescent coupling between adjacent waveguides in the array implies that the light traveling in a given waveguide can only tunnel to its nearest neighbor. These systems are ideal candidates for experimental investigations of $\mathcal{PT}$ symmetry breaking phenomena in lattice models [15,16,23]. In these systems, the tunneling is controlled by adjusting the separation between adjacent waveguides and the complex, on-site potential is determined by the local refractive index. The number of waveguides in a typical array is $N \sim 10 - 100$, and the experimental realizations correspond to a lattice with open boundary conditions. The tight-binding model, used widely in the field of condensed matter physics, is well suited for modeling such systems. The behavior of light traveling between adjacent waveguides is now described by a particle hopping on a lattice between nearest-neighbor sites. We begin this chapter by reviewing the properties of the tight-binding lattice in the absence of any impurities.

2.1 The Tight-Binding Model

The Hermitian Hamiltonian describing a particle hopping on a one-dimensional, N-site tight-binding lattice with open boundary conditions is given by

$$H = -t_0 \sum_{i=1}^{N-1} \left(a_{i+1}^\dagger a_i + a_i^\dagger a_{i+1} \right), \tag{2.1}$$

where $a_k^\dagger (a_k)$ is the creation (annihilation) operator for a state localized on the kth site, and $t_0 > 0$ is the tunneling amplitude between adjacent sites. A general single-

particle eigenfunction of the Hamiltonian can be written as $|\psi_k\rangle = \sum_{n=1}^{N} \psi_n^k |n\rangle$. The requirement that $H|\psi_k\rangle = E_k|\psi_k\rangle$ leads to

$$-t_0 \sum_{i=1}^{N-1} \left(a_{i+1}^\dagger a_i + a_i^\dagger a_{i+1} \right) \sum_{j=1}^{N} \psi_j^k |j\rangle = E_k \sum_{j=1}^{N} \psi_j^k |j\rangle \tag{2.2}$$

Since $a_i|j\rangle = \delta_{i,j}|0\rangle$, this becomes

$$-t_0 \sum_{i=1}^{N-1} \sum_{j=1}^{N} \psi_j^k \left(\delta_{i,j}|i+1\rangle + \delta_{i+1,j}|i\rangle \right) = E_k \sum_{j=1}^{N} \psi_j^k |j\rangle. \tag{2.3}$$

Further simplification, along with acting on both sides of the equation from the left with $\langle n|$, gives

$$-t_0 \left(\psi_{n+1}^k + \psi_{n-1}^k \right) = E_k \psi_n^k. \tag{2.4}$$

The coefficients ψ_n^k are given by the Bethe ansatz as $\psi_n^k = A\sin(kn) + B\cos(kn)$, and upon substitution into Eqn. (2.4) we arrive at the well-known $E_k = -2t_0\cos(k)$ energy band structure. Dirichlet boundary conditions require that the wavefunction vanish on sites $\{0, N+1\}$, restricting the eigenfunction coefficients to a sinusoidal form ($B = 0$) and giving N distinct values for the quasimomentum $k = \alpha\pi/(N+1)$, where $\alpha = 1, \ldots, N$. With these results in mind, we now add to the lattice two on-site $\mathcal{PT}$-symmetric potentials.

The non-Hermitian, $\mathcal{PT}$-symmetric potential V added to Eqn. (2.1) is given by

$$V = i\gamma(a_m^\dagger a_m - a_{\bar{m}}^\dagger a_{\bar{m}}). \tag{2.5}$$

The two impurities $(+i\gamma, -i\gamma)$ are located on mirror-symmetric sites $(m, \bar{m})$ with $1 \leq m \leq N/2$ and $\bar{m} = N + 1 - m$. A representation of the lattice is shown in Fig. 2.1. Note that the action of the parity operator for the lattice model is given by $\mathcal{P} a_n^\dagger \mathcal{P} = a_{\bar{n}}^\dagger$, and the action of the antilinear time-reversal operator is given by $\mathcal{T} i \mathcal{T} = -i$. Since the potential term V is odd under individual $\mathcal{P}$ and $\mathcal{T}$ operations, the Hamiltonian is $\mathcal{PT}$ symmetric. As in the case of the clean lattice, we can write

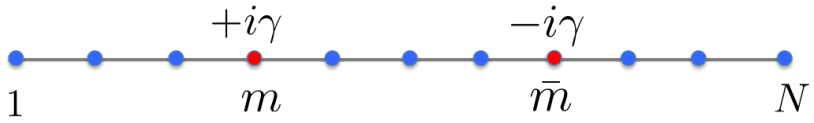

Fig. 2.1. A representation of an N-site tight-binding lattice where a particle is free to hop between nearest-neighbor sites in the presence of two $\mathcal{PT}$-symmetric impurities. The gain impurity $+i\gamma$ is located at site m, while the loss impurity $-i\gamma$ is located at the mirror-symmetric site $\bar{m} = N + 1 - m$. We only consider open boundary conditions in this chapter (i.e. the wavefunction vanishes on sites $\{0, N+1\}$).

the general single-particle eigenfunction $|\psi_k\rangle = \sum_{n=1}^{N} \psi_n^k |n\rangle$, where the coefficients ψ_n^k now have the form

$$\psi_n^k = \begin{cases} A\sin(kn), & n \leq m, \\ P\sin(kn) + Q\cos(kn), & m < n < \bar{m}, \\ B\sin(k\bar{n}), & n \geq \bar{m}. \end{cases} \tag{2.6}$$

Note that the coefficients are sinusoidal in the regions $n \leq m$ and $n \geq m$ since the wavefunction must vanish at sites $\{0, N+1\}$. By considering the eigenvalue equation at points $n = \{m, m+1\}$ and their reflection counterparts $n = \{\bar{m}, N-m\}$, we arrive at four equations governing the quasimomenta k, namely

$$\begin{aligned} -t_0\{P\sin[k(m+1)] &+ Q\cos[k(m+1)] + A\sin[k(m-1)]\} \\ &+ i\gamma A\sin(km) = -2t_0\cos(k)A\sin(km) \end{aligned} \tag{2.7}$$

$$\begin{aligned} -t_0\{P\sin[k(m+2)] &+ Q\cos[k(m+2)] + A\sin(km)\} \\ &= -2t_0\cos(k)\{P\sin[k(m+1)] + Q\cos[k(m+1)]\} \end{aligned} \tag{2.8}$$

$$\begin{aligned} -t_0\{B\sin(km) &+ P\sin[k(\bar{m}-1)] + Q\cos[k(\bar{m}-1)]\} \\ &- i\gamma B\sin(km) = -2t_0\cos(k)B\sin(km) \end{aligned} \tag{2.9}$$

$$\begin{aligned} -t_0\{B\sin(km) &+ P\sin[k(\bar{m}-2)] + Q\cos[k(\bar{m}-2)]\} \\ &- i\gamma B\sin(km) = -2t_0\cos(k)(P\sin[k(\bar{m}-1)] + Q\cos[k(\bar{m}-1)]) \end{aligned} \tag{2.10}$$

We cast these equations in matrix form and require the resulting 4×4 coefficient matrix to have determinant zero to ensure a non-trivial solution for $\{A, B, P, Q\}$. Ultimately, we find that the quasimomenta k obey the equation

$$\begin{aligned} M(k) &= \left\{ \sin^2[k(m+1)] + \left(\frac{\gamma^2}{t_0^2}\right) \sin^2(km) \right\} \\ &\quad \times \sin[k(N-2m+1)] + \sin^2(km) \\ &\quad \times \sin[k(N-2m-1)] - 2\sin(km) \\ &\quad \times \sin[k(m+1)] \sin[k(N-2m)] = 0. \end{aligned} \tag{2.11}$$

The $\mathcal{PT}$ symmetry is unbroken provided that Eqn. (2.11) has N real solutions. When $\gamma = 0$, the N distinct solutions are given by the well-known results for a tight-binding lattice with open boundary conditions, $k_\alpha = \alpha\pi/(N+1)$, where $\alpha = 1, \ldots, N$. Since $M(\pi - k) = (-1)^N M(k)$, if k_0 is a solution of Eqn. (2.11), then so is $(\pi - k_0)$. It also follows that when N is odd, $k = \pi/2$ is a solution irrespective of the value of γ and that the corresponding eigenvector has zero energy. When $m = 1$, Eqn. (2.11) reduces to the criterion for quasimomentum obtained in Ref. [24]; in that case, as $\gamma/t_0 \to 1$, the two central $k_\alpha \sim \pi/2$ become degenerate, the $\mathcal{PT}$ symmetry is spontaneously broken, and the system develops $N-2$ real and two complex (conjugate) eigenvalues.

Fig. 2.2(a) shows the typical plot of quasimomentum values $k(\gamma)/\pi$ as a function of γ for a lattice with $N = 20$ sites and the first impurity at $m = 4$ (solid red) or $m = 8$ (dashed blue). Since the plot is symmetric about $k = \pi/2$, we focus only on the left half $k/\pi \leq 0.5$ and note that since N is even, there is no solution present at $k = \pi/2$. As the impurity potential γ is increased, the adjacent quasimomenta and the corresponding energy levels become degenerate, leading to the $\mathcal{PT}$ symmetry breaking [24, 25]. We see that the critical potential for $m = 4$ is greater than that for $m = 8$, $\gamma_{\mathcal{PT}}(\mu = 0.2) > \gamma_{\mathcal{PT}}(\mu = 0.4)$, where $\mu = m/N$ is the relative position of the first impurity. In contrast with the $m = 1$ case, the two levels that become degenerate occur in a pair, with one near the origin $k \sim \pi/(N+1)$ and the other near the zone boundary $k \sim N\pi/(N+1)$. Therefore, when $\gamma(\mu) = \gamma_{\mathcal{PT}}(\mu) + 0^+$, there are four complex eigenvalues. We can define the "degree of $\mathcal{PT}$ symmetry

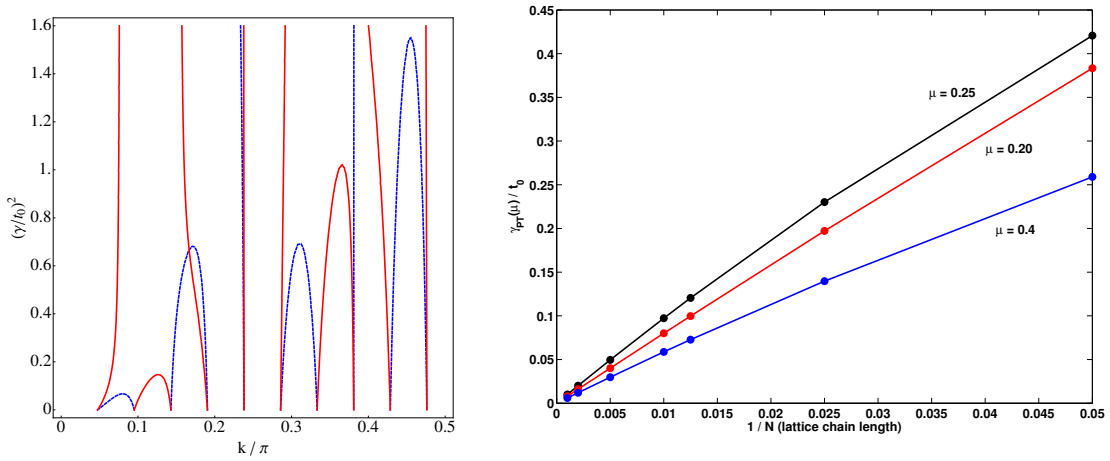

(a) (b)

Fig. 2.2. (a) The allowed values of quasimomenta k/π as a function impurity strength $(\gamma/t_0)^2$ for a lattice with $N = 20$ sites and the first impurity at $m = 4$ (solid red) or $m = 8$ (dashed blue). Because of the $\mathcal{PT}$-symmetric requirement, the plot is symmetric about $k = \pi/2$. $\mathcal{PT}$ symmetry breaking occurs when the two adjacent quasimomenta $k_1 \sim \pi/(N+1)$ and $k_2 \sim 2\pi/(N+1)$ become degenerate as $(\gamma/t_0)^2$ increases. (b) The critical potential strength $\gamma_{\mathcal{PT}}(\mu)/t_0$ as a function of the lattice size N for different positions $m = \mu N$ of the on-site potential. We see that $\gamma_{\mathcal{PT}}(\mu)$ vanishes as $N \to \infty$; therefore, the $\mathcal{PT}$-symmetric phase is algebraically fragile except when the impurities are the closest or the farthest.

breaking" as the fraction of eigenvalues that become complex. For a general m, as γ is increased beyond $\gamma_{\mathcal{PT}}$, we find that a total of $2m$ complex eigenvalues emerge and thus the degree of $\mathcal{PT}$ symmetry breaking is given by $2\mu \leq 1$. Fig. 2.2(b) shows the typical evolution of critical potential strength $\gamma_{\mathcal{PT}}(\mu)$ with N, for $\mu = \{0.2, 0.25, 0.4\}$, obtained by numerically solving Eqn. (2.11). The scaling suggests that the critical potential strength for the infinite lattice approaches zero, $\gamma_{\mathcal{PT}}(\mu) \propto 1/N \to 0$. We define the $\mathcal{PT}$-symmetric phase as robust (fragile) provided the critical impurity strength $\gamma_{\mathcal{PT}}(N)$, below which all eigenvalues are real, is nonzero (zero) in the limit $N \to \infty$. Thus, the $\mathcal{PT}$-symmetric phase, which exists in the region $0 \leq \gamma \leq \gamma_{\mathcal{PT}}$, is algebraically fragile. This result can be qualitatively understood as follows: in the limit $N \gg 1$ and $m \gg 1$ with $m/N = \mu$, Eqn. (2.11) can be approximated by $\gamma^2 \sin[(1-2\mu)kN] = 0$. If $\gamma \neq 0$, this equation has only $N(1-2\mu) < N$ real solutions, and hence the $\mathcal{PT}$ symmetry is broken. We emphasize that this argument is invalid when $\mu \to 0$ and the corresponding critical potential is given by $\gamma_{\mathcal{PT}}(\mu) = t_0$ [24]. It is also invalid when $\mu \to 1/2$, when the impurities are closest to each other and, as we discuss below, the critical $\gamma_{\mathcal{PT}}(\mu)$ is nonzero when $N \to \infty$.

2.2 Closest Impurities and the Even-Odd Effect

We now consider the case of closest impurities. Note that due to the $\mathcal{PT}$-symmetric requirement, when N is even the impurities are nearest neighbors with $m = N/2$, whereas when N is odd the impurities are next-to-nearest neighbors with $m = (N-1)/2$. We will first focus on the case with an even N. In this case, the condition $M(k) = 0$ from Eqn. (2.11) reduces to the following equation

$$t_0^2 \sin^2\left[k\left(\frac{N}{2}+1\right)\right] = (t_0^2 - \gamma^2)\sin^2\left(\frac{kN}{2}\right). \tag{2.12}$$

When $\gamma = 0$ Eqn. (2.12) has N distinct solutions given by $k_\alpha = \alpha\pi/(N+1)$. As γ increases the adjacent k_α approach each other and when $\gamma = t_0$, Eqn. (2.12) has $N/2$ doubly degenerate solutions given by $k_n = 2n\pi/(N+2)$, where $n = 1, \ldots, (N/2)$. When $\gamma > t_0$, it is clear that Eqn. (2.12) has no real solutions. Thus the $\mathcal{PT}$ symmetry

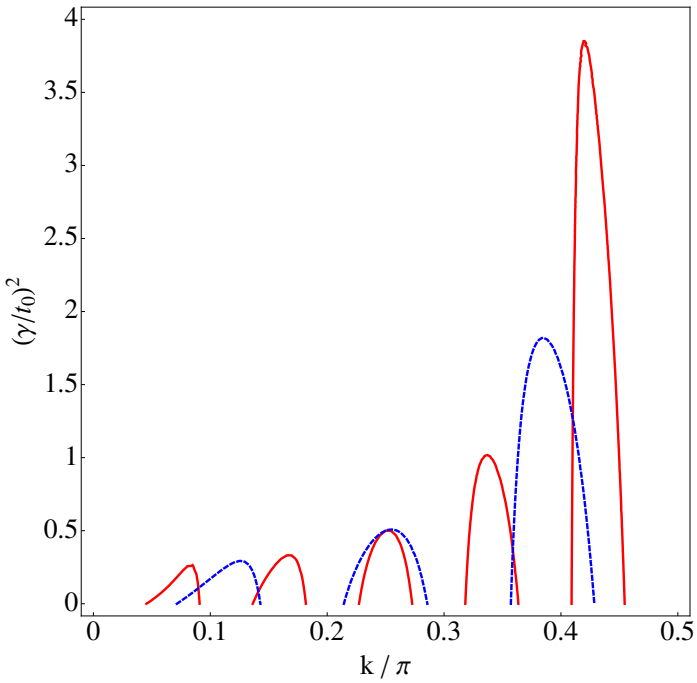

Fig. 2.3. Allowed quasimomenta $k(\gamma)/\pi$ for a lattice with $N = 21$ (red line) and $N = 13$ (dashed blue line) sites as a function of potential strength $(\gamma/t_0)^2$ when the impurities are closest to each other. As $N \to \infty$, we find that the critical potential strength $\gamma_{\mathcal{PT}} \to t_0/2$.

is maximally broken and all N eigenvalues simultaneously become complex. When N is odd, the impurities are at sites $N_0 \pm 1$, where $N_0 = (N+1)/2$ is the site at the center of the lattice. The equation $M(k) = 0$ then reduces to

$$\cos(k)\left\{\sin^2(kN_0) + \left(\frac{\gamma^2}{t_0^2}\right)\sin^2[k(N_0-1)]\right\} = \sin(kN_0)\sin[k(N_0-1)]. \qquad (2.13)$$

This equation has all real solutions provided $\gamma/t_0 \leq 1/(2\cos k_d)$, where $\pi/(N+1) < k_d < 2\pi/(N+1)$ corresponds to the first degenerate quasimomentum. Therefore, we find that as the γ is increased from zero the $\mathcal{PT}$ symmetry breaks at $\gamma_{\mathcal{PT}} = t_0/2$ in the limit $N \to \infty$ when adjacent k_α near the origin become degenerate. Hence, for $\gamma = \gamma_{\mathcal{PT}} + 0^+$, there are four complex eigenvalues. On the other hand, Eqn. (2.13) has only one real solution, $k = \pi/2$, when $\gamma/t_0 > 1/(2\cos k_D)$, where $k_D \leq \pi/2$ is the degenerate quasimomentum closest to the zone center $k = \pi/2$. Hence, the number of complex eigenvalues increases monotonically and when $\gamma > t_0/(2\cos k_D) \sim$

$t_0(N+1)/3\pi$, it saturates to $2m = N-1$. Fig. 2.3 shows the quasimomenta $k_\alpha(\gamma)$ for a lattice with $N = 13$ and $N = 21$ sites obtained from Eqn. (2.13) and confirms these results. Since the $\mathcal{PT}$-symmetric nature of the potential dictates the minimum distance between the impurities when N is odd or even, the phase diagram of the lattice is sensitive to it even as $N \to \infty$.

2.3 Numerical Results

We start this section with numerical results for the critical potential strength $\gamma_{\mathcal{PT}}(\mu)$ as a function of the relative impurity site location $0 < \mu = m/N \leq 1/2$ obtained by numerical diagonalization of the Hamiltonian for various lattice sizes N, even and odd. The left panel in Fig. 2.4 shows that, for an even N, apart from the finite-size effects that are prominent near $\mu = 1/4$ and are also present in solutions to Eqn. (2.11), the critical potential strength $\gamma_{\mathcal{PT}}(\mu)$ is vanishingly small except at $\mu = 1/N$ and $\mu = 0.5$. In both special cases $\gamma_{\mathcal{PT}} = t_0$. The right panel in the same figure shows results for odd N. When $\mu = 1/N$ we recover the result

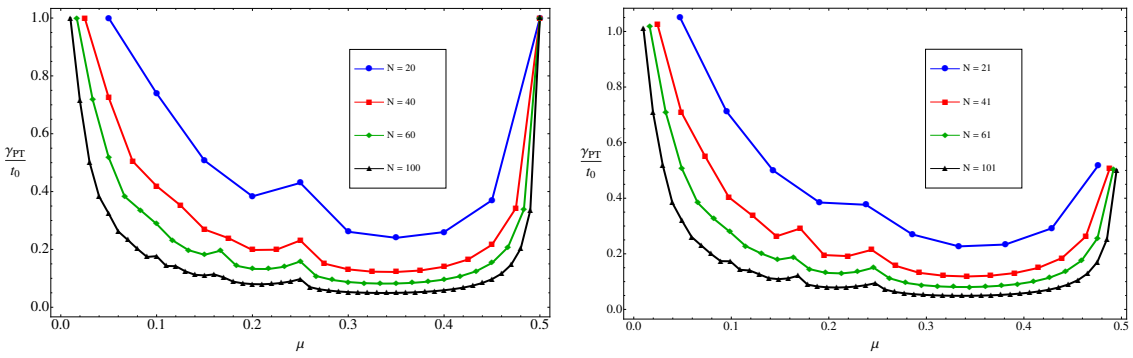

(a) (b)

Fig. 2.4. (a) $\gamma_{\mathcal{PT}}/t_0$ vs. $\mu = m/N \leq 1/2$ for an even-N lattice. As N increases $\gamma_{\mathcal{PT}}(\mu)$ decreases, except when the impurities are farthest ($\mu = 1/N$) or the closest ($\mu = 1/2$). At the endpoints $\gamma_{\mathcal{PT}} = t_0$ is independent of N. (b) The results are similar except for when the impurities are the closest, in which case $\gamma_{\mathcal{PT}} = t_0/2$ as $N \to \infty$.

$\gamma_{\mathcal{PT}} = t_0\sqrt{1+2/(N-1)}$ [24]. As in the case with even N, we find that the $\gamma_{\mathcal{PT}}(\mu)$ is suppressed with increasing N everywhere except when $\mu = 0.5 - 1/(2N)$ or equivalently $m = (N-1)/2$. These results are consistent with those obtained through the analytical treatment earlier. We now briefly explore the change in a typical dimensionless eigenfunction $\psi_k(n)$ as a function of impurity potential γ in the case of nearest-neighbor impurities (even N). In the $\mathcal{PT}$-symmetric phase, an eigenfunction is given by $\psi_<(n) = A\sin(kn)$ for $n \leq N/2$ and $\psi_>(n) = B\sin(k\bar{n})$ for $n > N/2$, where k is a quasimomentum that satisfies Eqn. (2.12). Using the eigenfunction constraints and Eqn. (2.12) it follows that

$$B = A\left\{\frac{\sin[k(1+N/2)]}{\sin(kN/2)} + i\frac{\gamma}{t_0}\right\} = A\exp(i\theta_\gamma), \tag{2.14}$$

where the angle θ_γ satisfies $\tan\theta_\gamma = \gamma\sin(kN/2)/t_0\sin[k(1+N/2)]$. Fig. 2.5 shows the amplitude $|\psi_k(n)|$ and the phase $\Phi(n)$ of the ground-state wave function of a lattice with $N = 20$ sites and nearest neighbor impurities. The top (blue) panel shows that when $\gamma = \gamma_{\mathcal{PT}} = t_0$, the wave function amplitude is even about the center of the lattice and the phase is given by $\theta_\gamma = \pi/2$, as is expected from Eqn. (2.14). The bottom (red) panel shows that when $\gamma = 1.01t_0 > \gamma_{\mathcal{PT}}$, the broken $\mathcal{PT}$ symmetry is reflected in the asymmetrical wave-function amplitudes and in the position-dependent phase factor $\Phi(n)$. These are generic features of the broken $\mathcal{PT}$ symmetry phase. We also note that in the continuum limit, the eigenfunction $\psi_k(x)$ becomes discontinuous at the center of the lattice while the probability amplitude $|\psi_k(x)|$ remains continuous.

2.4 Conclusions

We have investigated the phase diagram of an N-site one-dimensional lattice with a pair of complex $\mathcal{PT}$-symmetric impurities located at sites $\{m, \bar{m}\}$ within it. A remarkable feature of such a Hamiltonian is that in the $\mathcal{PT}$-symmetric region, its spectrum remains confined within the energy band $\pm 2t_0$ of the model in the absence of impurities; as the impurity potential γ is increased, the level spacing between adjacent energy levels decreases. Our results show that the $\mathcal{PT}$-symmetric phase of

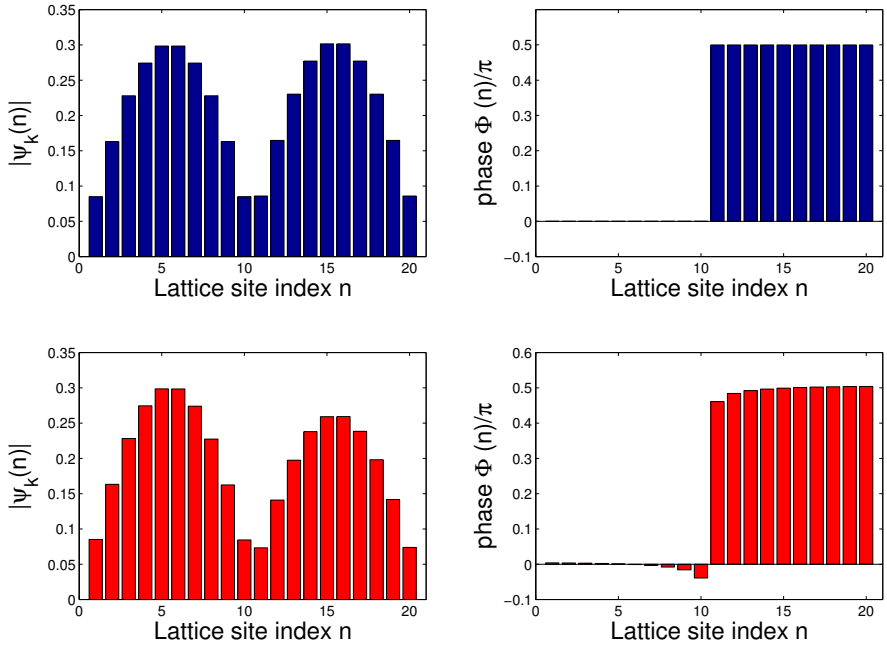

Fig. 2.5. The top (blue) panel shows the amplitude $|\psi_k(n)|$ (left) and the phase $\Phi(n)/\pi$ (right) of the dimensionless ground-state wave function of a $\mathcal{PT}$-symmetric lattice with $N = 20$ sites and nearest-neighbor impurities with strength $\gamma = \gamma_{\mathcal{PT}} = t_0$. As is expected of a $\mathcal{PT}$-symmetric state, the amplitude is even around the center of the lattice, and the effect of a nonzero γ is manifest in the discontinuous change in the phase, with $\Phi(n) = 0$ for $n \leq N/2$ and $\Phi(n) = \pi/2$ for $n > N/2$, consistent with Eqn. (2.12). The bottom (red) panel shows the same state when $\gamma/t_0 = 1.01$ and the $\mathcal{PT}$ symmetry is spontaneously broken. The broken symmetry is manifest in the asymmetrical wave function amplitude (left) and a position-dependent phase $\Phi(n)$.

such a lattice is algebraically fragile except when the impurities are farthest from each other or are closest to each other. In the latter case, we find that the $\mathcal{PT}$-symmetric phase survives when $\gamma \leq \gamma_{\mathcal{PT}} = t_0$ (even N) or $\gamma \leq \gamma_{\mathcal{PT}} = t_0/2$ (odd N). We note that such a lattice offers tremendous tunability due to its variable critical impurity strength $\gamma_{\mathcal{PT}}(\mu)$ for a finite N, and the corresponding variable fraction of complex eigenvalues 2μ, which translates into the number of dissipative channels in both classical [16] and quantum systems. Thus, a physical realization of such a

model [26] may offer the ability to engineer the level spacings and the dissipation in this system. In Chapter 3, we will show how the results for a one-dimensional lattice differ substantially from those of a $\mathcal{PT}$-symmetric ring. In particular, we see how periodic boundary conditions lead to an insensitivity to impurity location on the critical impurity strength, in stark contrast to the results for a chain.

3. $\mathcal{PT}$ SYMMETRY BREAKING IN UNIFORM RINGS

In this chapter, we explore the effects of $\mathcal{PT}$ symmetry breaking in a ring-lattice with of a pair of non-Hermitian impurities $\pm i\gamma$. Note that because of the periodic boundary conditions (PBCs) of a ring (i.e. site 1 coincides with site $N+1$), such a pair of impurities represents $\mathcal{PT}$-symmetric impurities irrespective of the individual impurity locations; in other words, for given impurity locations, a parity operator can be defined such that the impurity Hamiltonian becomes $\mathcal{PT}$ symmetric. The lattice is characterized by two tunneling amplitudes that are uniform along the two paths that connect the impurities but may be different from each other.

3.1 The Modified Tight-Binding Model

We start with a one-dimensional lattice with N sites and PBCs. Without loss of generality, we take the gain and loss impurities $(i\gamma, -i\gamma)$ at positions $(1, d)$ where $2 \leq d \leq N$. The Hamiltonian for this lattice is given by $H_{\mathcal{PT}} = H_0 + V$, where the Hermitian tunneling Hamiltonian H_0 is given by

$$H_0 = -\sum_{i=1}^{N} t(i)(a_{i+1}^{\dagger} a_i + a_i^{\dagger} a_{i+1}), \tag{3.1}$$

$$t(i) = \begin{cases} t_b > 0, & 1 \leq i < d, \\ t_0 > 0, & d \leq i \leq N. \end{cases} \tag{3.2}$$

Here $t(j)$ is the tunneling amplitude between adjacent sites j and $j+1$, $a_j^{\dagger}$ (a_j) is the creation (annihilation) operator for a single-particle state $|j\rangle$ localized at site j, and PBCs imply that $a_{N+1}^{\dagger} = a_1^{\dagger}$. A representation of the lattice is shown in Fig. 3.1. The $\mathcal{PT}$-symmetric, non-Hermitian potential is given by

$$V = i\gamma(a_1^{\dagger} a_1 - a_d^{\dagger} a_d) \neq V^{\dagger}. \tag{3.3}$$

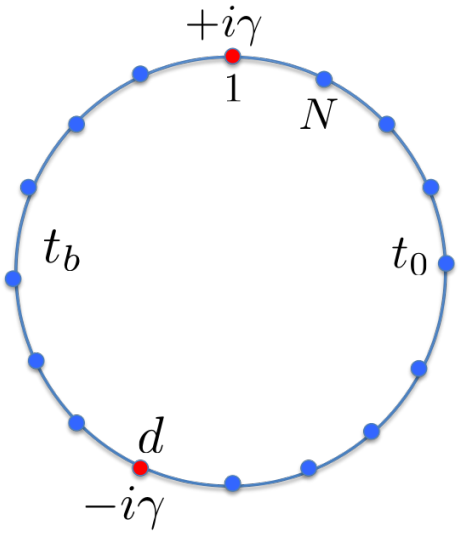

Fig. 3.1. A representation of an N-site tight-binding ring where a particle is free to hop between nearest-neighbor sites in the presence of two $\mathcal{PT}$-symmetric impurities. The gain impurity $+i\gamma$ is located at site 1, while the loss impurity $-i\gamma$ is located at site d. The tunneling between sites 1 and d is uniform and given by t_b, while outside this region it is given by t_0. A ring implies periodic boundary conditions, meaning that the sites $\{1, N+1\}$ coincide.

When $\gamma = 0$, the energy spectrum of the Hamiltonian $H_{\mathcal{PT}}$ is given by $E(k,k') = -2t_0\cos(k) = -2t_b\cos(k')$ and is bounded by $2\max(t_0,t_b)$. When $t_0 \geq t_b$, the N eigenmomenta correspond to purely real k values and k' values that are either real or purely imaginary; when $t_0 \leq t_b$, the situation is reversed [27]. When $\gamma \neq 0$, since the tunneling amplitudes along the two paths between the gain and loss impurities are constant, an arbitrary eigenfunction $|\psi\rangle = \sum_j f(j)|j\rangle$ with energy $E(k,k')$ can be expressed using the Bethe ansatz as [24, 27]

$$f(n) = \begin{cases} A\sin(k'n) + B\cos(k'n), & 1 \leq n \leq d, \\ P\sin(kn) + Q\cos(kn), & d+1 \leq n \leq N. \end{cases} \tag{3.4}$$

To obtain the dimensionless quasimomentum k (or, equivalently, k'), we consider the eigenvalue equations at impurity locations and their neighboring sites,

$$\begin{aligned} t_0[P\sin(kN)+Q\cos(kN)] &+ t_b[A\sin(2k')+B\cos(2k')] \qquad (3.5)\\ &= -(E-i\gamma)[A\sin(k')+B\cos(k')] \\ t_0\{P\sin[k(N-1)]+Q\cos[k(N-1)] &+ A\sin(k')+B\cos(k')\} \qquad (3.6)\\ &= -E[P\sin(kN)+Q\cos(kN)] \\ t_b\{A\sin[k'(d-1)]+B\cos[k'(d-1)]\} &+ t_0\{P\sin[k(d+1)] \qquad (3.7)\\ +Q\cos[k(d+1)]\} &= -(E+i\gamma)[A\sin(k'd)+B\cos(k'd)] \\ t_b\{P\sin[k(d+2)]+Q\cos[k(d+2)] &+ A\sin(k'd)+B\cos(k'd)\} \qquad (3.8)\\ &= -E\{P\sin[k(d+1)]+Q\cos[k(d+1)]\} \end{aligned}$$

As in Chapter 2, we cast these four equations in matrix form and require the resulting 4×4 coefficient matrix to have determinant zero to ensure a non-trivial solution for $\{A,B,P,Q\}$. The resulting characteristic equation for the quasimomenta is then given by

$$\begin{aligned} M(k,k') \equiv\ & t_0^2\sin[k'(d-1)]\sin[k(N-d-1)] \\ & +t_b^2\sin[k'(d+1)]\sin[k(N-d+1)] \\ & -2t_bt_0\{\sin(k'd)\sin[k(N-d)]+\sin(k')\sin(k)\} \\ & +\gamma^2\sin[k'(d-1)]\sin[k(N-d+1)]=0. \qquad (3.9) \end{aligned}$$

It is easy to check the following properties of the quasimomenta that follow from Eqn. (3.9). When $t_0\geq t_b$, the real quasimomenta k are constrained by $-\pi<k\leq\pi$. Then the states with quasimomenta k and $-k$ are degenerate except when $k=0,\pi$, provided the corresponding k' is purely real. If k_0 is a real quasimomentum, then $\pi-k_0$ is also a quasimomentum if and only if N is even; when $t_0\leq t_b$, the situation is reversed. Thus in contrast with an open lattice, the spectrum of a lattice with PBCs has a particle-hole symmetric spectrum if and only if N is even. Fig. 3.2 shows the numerically-obtained typical phase diagram for the critical impurity strength $\gamma_{\mathcal{PT}}$ as

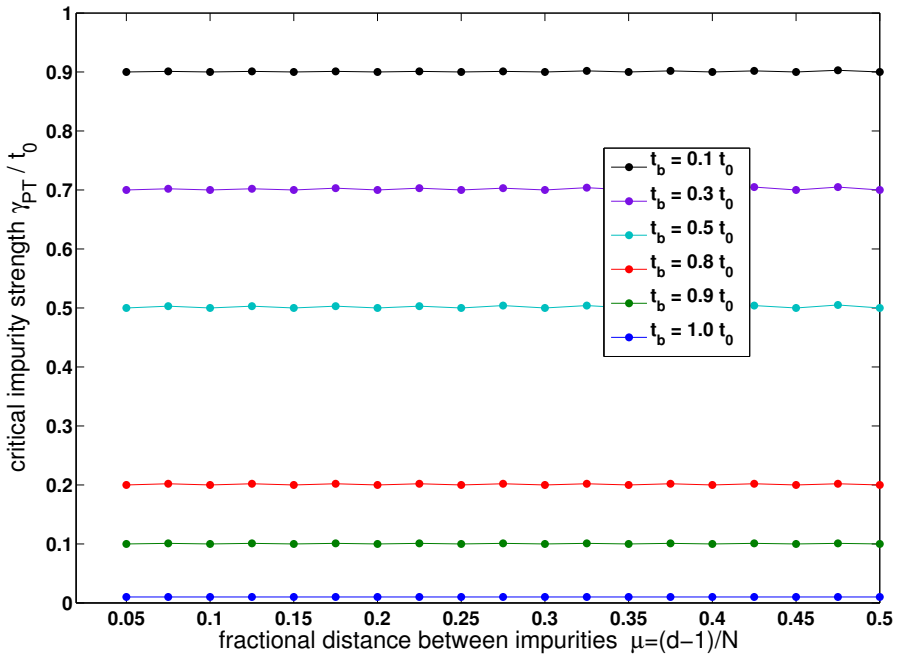

Fig. 3.2. Typical $\mathcal{PT}$ phase diagram of a lattice with PBCs. These results are for a lattice with $N = 40$, $t_0 = 1$, and impurities $\pm i\gamma$ at sites $(1, d)$ for different values of the sink position d and different $t_b \leq t_0$; we get identical results for odd N or $t_b > t_0$. Remarkably, the critical impurity strength $\gamma_{\mathcal{PT}}(\mu) = |t_0 - t_b|$ is independent of the distance μ between the impurities; for small $N \leq 10$, this is not true.

a function of the fractional distance between impurities $\mu = (d-1)/N$. Note that since there are two paths from the source $i\gamma$ to the sink $-i\gamma$, we restrict the fractional distance to $0 \leq \mu \leq 1/2$. These results are obtained for a lattice with $N = 40$, $t_0 = 1$, and $t_b \leq t_0$. We obtain identical results for odd N and different values of tunneling amplitudes including $t_b > t_0$ when the impurity strength γ is measured in units of $\max(t_0, t_b)$. We also find that the weak μ dependence of the critical impurity strength $\gamma_{\mathcal{PT}}/\max(t_0, t_b)$ vanishes as N increases.

This remarkable phase diagram predicts that in a lattice with PBCs, the critical impurity strength $\gamma_{\mathcal{PT}}(\mu)$ is independent of the interimpurity distance μ and is given by $\gamma_{\mathcal{PT}} = |t_b - t_0|$. It implies that the fragile $\mathcal{PT}$-symmetric phase in an open lattice with constant tunneling [25, 28] is stabilized and strengthened by PBCs and that the critical impurity strength $\gamma_{\mathcal{PT}}$ can be easily tuned by an appropriate choice of tunneling amplitudes.

To gain insight into the insensitivity of $\gamma_{\mathcal{PT}}(\mu)$ to the interimpurity distance μ for large $N \gg 1$, let us consider Eqn. (3.9) in the limit $1 \ll d \ll N$,

$$\frac{\sin(k'\mu N)\sin[k(1-\mu)N]}{\sin(k')\sin(k)} = \frac{2t_0 t_b}{[(t_0 - t_b)^2 + \gamma^2]} \tag{3.10}$$

We remind the reader that, similar to the characteristic Eqn. (3.9), Eqn. (3.10) represents two distinct equations based on when k' is purely real or purely imaginary [27]. Since we have chosen, without loss of generality, $t_b \leq t_0$, k is always purely real. Thus, investigating the graphical solutions of Eqn. (3.10) requires some care. As γ increases, we find that two adjacent quasimomenta near $k \sim \pi/2$ become degenerate and then complex, leading to $\mathcal{PT}$ symmetry breaking. Note that when $k \sim \pi/2$, the eigenenergy is low, $E(k, k') = -2t_0\cos(k) \leq \min(t_0, t_b)$, and thus the corresponding eigenmomentum $k' = \arccos(E/t_b) \sim \pi/2$ is purely real. Therefore, to determine the $\mathcal{PT}$-breaking threshold $\gamma_{\mathcal{PT}}(\mu)$, we only focus on these quasimomenta; a graphical solution in this vicinity then shows that $\gamma_{\mathcal{PT}}$ is independent of the fractional interimpurity distance μ.

3.2 Wave Function and Momentum Evolution

Now we consider the real- and reciprocal-space time evolution of a wave packet that is initially localized on a single site. In an optical-waveguide realization of a $\mathcal{PT}$-symmetric system, this initial state is most easily achievable. In such a system, the wave function $|\psi(t)\rangle$ represents single-transverse-mode electric fields in each waveguide, their classical dynamics are identical to that of a quantum particle on a tight-binding lattice [19], and the time evolution is not unitary since, based on its engineering, a waveguide can absorb or emit light, thus violating unitarity [15,16,23]. For an arbitrary, normalized initial state $|\psi(0)\rangle$, the wave function at time t is given by $|\psi(t)\rangle = \exp(-iH_{PT}t/\hbar)|\psi(0)\rangle$, and the time evolution operator $\exp(-iH_{PT}t/\hbar)$ is not unitary since the Hamiltonian $H_{\mathcal{PT}}$ is not Hermitian. We denote the site- and time-dependent real-space intensity by $I_R(j,t) = |\langle j|\psi(t)\rangle|^2$, where $j = 1,\ldots,N$ denotes the site index, and use $I_M(u,t) = |\langle u|\psi(t)\rangle|^2$ to denote the reciprocal-space intensity where the discrete index $u = 1,\ldots,N$ corresponds to the reciprocal-space index $p_u = \pi(2u/N - 1)$ with $-\pi < p_u \leq \pi$.

The left-hand column in Fig. 3.3 shows the typical evolution of real-space intensity with increasing impurity strength. For a detailed description of how these plots are generally calculated, see Appendix B. These results are for a lattice with $N = 32$, $t_0 = 0.5$, $t_b = 1.0$, the source and sink at sites 1 and $d = 16$, respectively, and the initial wave packet localized at site $m_0 = 8$. The vertical axis in each panel indicates the site index, and the horizontal axis denotes time measured in units of $2\pi\hbar/\max(t_0, t_b)$. When $\gamma = 0$ (top panel), the wave packet diffuses, suffering a change in speed at the impurity locations consistent with the change in the tunneling amplitude. This amounts to a statement of the conservation of momentum. In the central panel, the slope of the orange lines overlaid in each of the two tunneling regions gives the speed of the wave packet in the respective region. We then multiply each speed by the appropriate effective mass ($m_{eff} = \hbar^2/(2ta^2)$), where t is the tunneling parameter in the relevant region and a is the lattice spacing. We find that $p_1 = 0.89\hbar^2/a$

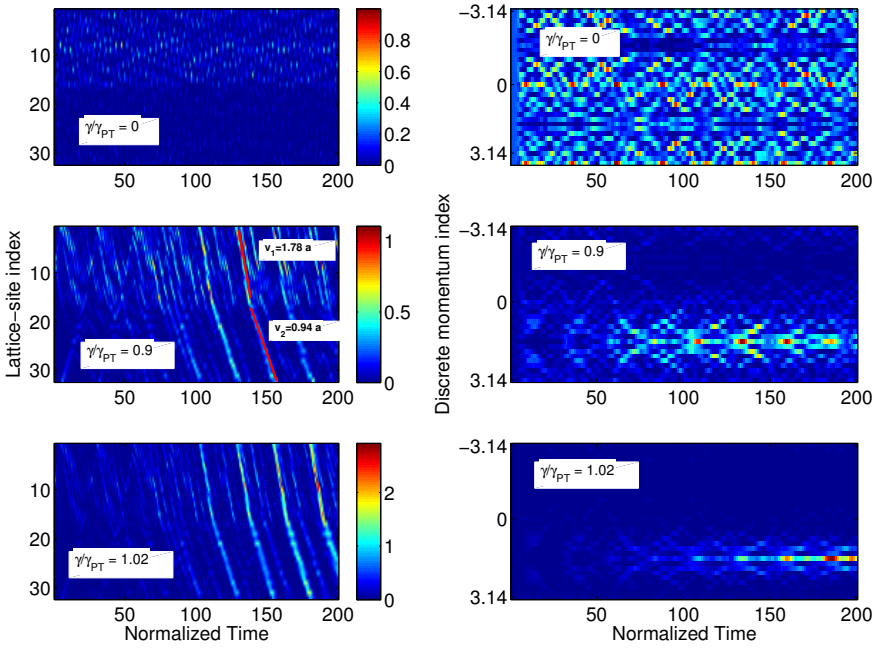

Fig. 3.3. Left: Evolution of real-space intensity $I_R(j,t)$ with increasing $\gamma \geq 0$ in an $N = 32$ lattice with impurities $\pm i\gamma$ at sites 1 and 16, $t_0 = 0.5$, $t_b = 1.0$, and the initial wave packet localized at site $m_0 = 8$. When $\gamma = 0$ the wave picket diffuses without preferential chirality. As γ increases towards $\gamma_{\mathcal{PT}}$ (center panel) and beyond (bottom panel), the wave function evolution becomes chiral. Recall that due to PBCs, the bottom-most lattice site in each panel is connected with the top-most lattice site. Right: The corresponding reciprocal-space intensity $I_M(u,t)$. The vertical axis corresponds to the reciprocal-space index $-\pi < p_u \leq \pi$. As γ increases, we see that the reciprocal-space intensity develops a clear peak at a finite, positive value of p_u, consistent with the real-space motion of the wave packet in the left column.

and $p_2 = 0.94\hbar^2/a$, which within the error due to visual inspection, indicates that the momentum is indeed conserved. As γ increases towards $\gamma_{\mathcal{PT}}$ (center panel) and beyond (bottom panel), the wave packet evolution acquires a chirality and the overall intensity also increases from its $\gamma = 0$ value. In an open lattice, there is only one path from the source to the sink: in contrast, a lattice with PBCs has two such paths. Physically, the chirality implies that, on average, the path with the higher tunneling amplitude is preferred over the other only when $\gamma > 0$. Note that this does not represent a preferential flow from source to the sink – the wave packet motion continues past the sink to the source again – but, rather, the handedness of the motion in the position-time plane [29]. We also emphasize that when $\gamma = 0$ (top panel), on average, both paths are equally preferred. These results are robust, independent of the initial location m_0 of the wave packet, the distance $(d-1)$ between the impurities, and the lattice tunneling parameters.

The right-hand column in Fig. 3.3 provides a complementary view with the corresponding evolution of the reciprocal-space intensity $I_M(u,t)$. The vertical axis in each panel corresponds to the reciprocal-space index $p_u \in (-\pi, \pi]$. The top panel shows that when $\gamma = 0$, as the wave packet diffuses, its average momentum is 0. As γ approaches $\gamma_{\mathcal{PT}}$ (center panel) and beyond (bottom panel), we see that the reciprocal-space intensity develops a pronounced peak at a finite, positive value, consistent with the preferential flow shown in the left-hand column. In addition, results at longer times, $T \sim 10N \gg N$, show that the reciprocal-space intensity distribution for $\gamma > 0$ reaches a steady state.

To quantify this effect and to dissociate it from the exponentially increasing net intensity $I_R(t) = \sum_j I_R(j,t)$ that occurs for $\gamma > \gamma_{\mathcal{PT}}$ [30], we develop a dimensionless, discrete momentum operator on the lattice with PBCs (i.e. the lattice analog of

$p = -i\hbar\partial_x$). We begin by recalling the proof demonstrating that the momentum p is a Hermitian operator, namely

$$\begin{aligned}
\langle f|p|g\rangle &= \langle f| \left(\int dx|x\rangle\langle x| \right) p \left(\int dx'|x'\rangle\langle x'| \right) g\rangle \\
&= \int dx \int dx' \langle f|x\rangle\langle x|p|x'\rangle\langle x'|g\rangle \\
&= \int dx \int dx' f^*(x)[-i\hbar\partial_x \delta_{x,x'}]g(x') \\
&= -i\hbar \int dx f^*(x)\partial_x g(x) \qquad (3.11)
\end{aligned}$$

And upon integrating by parts we get

$$\begin{aligned}
\langle f|p|g\rangle &= -i\hbar f^*(x)g(x)\big|_{\text{boundary}} + i\hbar \int dx g(x)\partial_x f^*(x) \\
&= -i\hbar f^*(x)g(x)\big|_{\text{boundary}} + \int dx g(x)(-i\hbar\partial_x f(x))^* \\
&= -i\hbar f^*(x)g(x)\big|_{\text{boundary}} + \left\{ \int dx g^*(x)(-i\hbar\partial_x f(x)) \right\}^* \\
&= -i\hbar g^*(x)g(x)\big|_{\text{boundary}} + (\langle g|p|f\rangle)^* \qquad (3.12)
\end{aligned}$$

At this point, the boundary term is usually set to zero since the wave function vanishes at the boundaries, but we leave it intact to compare with the discrete case. Since the derivative takes the form of a finite difference in the discrete case, the question arises whether to use the forward difference $\langle f|p|g\rangle \equiv -i\hbar \sum_{k=1}^{N} f^*(k)(g_{k+1} - g_k)$ or the backward difference $\langle f|p|g\rangle \equiv -i\hbar \sum_{k=2}^{N+1} f^*(k)(g_k - g_{k-1}) = -i\hbar \sum_{k=1}^{N} f^*_{k+1}(g_{k+1} - g_k)$. We opt to use their average, and check whether the result is Hermitian:

$$\langle f|p|g\rangle \equiv -\frac{i\hbar}{2} \sum_{k=1}^{N} \left(f_k^* + f_{k+1}^*\right)(g_{k+1} - g_k) \qquad (3.13)$$

So we must verify that $\langle f|p|g\rangle = (\langle g|p|f\rangle)^*$. By definition, we have

$$(\langle g|p|f\rangle)^* = \left\{ -\frac{i\hbar}{2} \sum_{k=1}^{N} \left(g_k^* + g_{k+1}^*\right)(f_{k+1} - f_k) \right\}^*, \qquad (3.14)$$

and upon expanding we get

$$(\langle g|p|f\rangle)^* = \frac{i\hbar}{2} \sum_{k=1}^{N} (f_{k+1}^* g_{k+1} - f_k^* g_k + f_{k+1}^* g_k - f_k^* g_{k+1}). \qquad (3.15)$$

We reorder the summations and group the boundary terms together as

$$\begin{aligned}(\langle g|p|f\rangle)^* &= -i\hbar(f_1^* g_1 - f_{N+1}^* g_{N+1}) - \frac{i\hbar}{2}\sum_{k=1}^{N}(f_{k+1}^* g_{k+1} - f_{k+1}^* g_k + f_k^* g_{k+1} - f_k^* g_k), \\ &= -i\hbar(f_1^* g_1 - f_{N+1}^* g_{N+1}) - \frac{i\hbar}{2}\sum_{k=1}^{N}\left(f_k^* + f_{k+1}^*\right)(g_{k+1} - g_k) \qquad (3.16)\end{aligned}$$

So we finally arrive at the expression

$$\langle f|p|g\rangle = i\hbar(f_1^* g_1 - f_{N+1}^* g_{N+1}) + (\langle g|p|f\rangle)^* \qquad (3.17)$$

Because of the PBCs, $f_1 = f_{N+1}$, therefore the boundary terms cancel and the discrete momentum operator is Hermitian. So the final expression for the discrete momentum operator (considering the time evolution), is given by

$$\langle f(t)|p|g(t)\rangle = -\frac{i\hbar}{2}\sum_{j=1}^{N}\frac{(f_{j+1}^* + f_j^*)(g_{j+1} - g_j)}{\sqrt{\langle f|f\rangle\langle g|g\rangle}}, \qquad (3.18)$$

where $|f(t)\rangle = \sum_j f_j(t)|j\rangle$, $|g(t)\rangle = \sum_j g_j(t)|j\rangle$, and the normalization factor in the denominator is necessary due to the non unitary time evolution. As suggested by the right-hand column in Fig. 3.3, the momentum expectation value $p_f(t) = \langle f(t)|p|f(t)\rangle$ in a given state oscillates about 0 when $\gamma = 0$ and reaches a steady-state value $p(\gamma) \equiv \int_0^T p(t')dt'/T$ when $\gamma > 0$. Since $|p_f(t)| \leq 1$ for any initial state and time, the magnitude of $p(\gamma)$ is bounded by unity.

Fig. 3.4 shows the typical evolution of the dimensionless, steady-state momentum $p(\gamma)$ across the $\mathcal{PT}$-symmetry-breaking threshold for different locations of the loss impurity. These results are for a lattice with $N = 32$, $t_0 = 0.5$, $t_b = 1$, and thus, $\gamma_{\mathcal{PT}}/\max(t_0, t_b) = 0.5$. The initial location of the wave packet is $m_0 = 10$, and we have used normalized time $T = 500$ to numerically obtain the average. When $\gamma = 0$, $p(\gamma) = 0$, and at small γ, we see that the $p(\gamma)$ increases linearly with γ; the slope of this line increases monotonically with d. We find that the steady-state momentum reaches a universal value, $p = 1$, at the $\mathcal{PT}$-breaking point and decreases linearly for $\gamma \geq \gamma_{\mathcal{PT}}$. Thus, although the total intensity increases exponentially with time, the momentum, which captures the handedness of motion of the wave packet, decreases

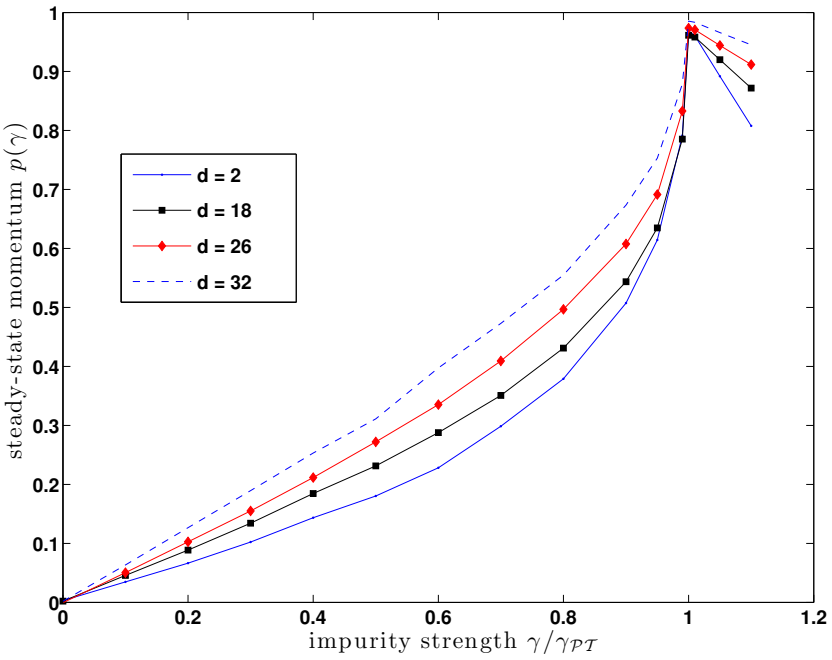

Fig. 3.4. Dependence of the steady-state momentm $p(\gamma)$ as a function of the impurity strength γ for different locations d of the loss impurity $-i\gamma$; the gain impurity $i\gamma$ is located at site 1. The initial wave function is localized at site $m_0 = 10$. The momentum $p(\gamma)$ varies linearly with γ at small $\gamma/\gamma_{\mathcal{PT}} \ll 1$. It reaches a universal, maximum value, $p = 1$, at the $\mathcal{PT}$-symmetry-breaking threshold. For $\gamma/\gamma_{\mathcal{PT}} \gg 1$, the steady-state momentum decreases, although the net intensity increases exponentially with time.

for $\gamma > \gamma_{\mathcal{PT}}$. The maximal value of $p(\gamma)$ at the threshold $\gamma = \gamma_{\mathcal{PT}}$ is a robust feature, observed universally in tight-binding lattices with a single pair of $\mathcal{PT}$-symmetric impurities, irrespective of the tunneling profile, the distance between the impurities, and the initial location of the wave packet.

3.3 Conclusions

In this section, we have investigated the $\mathcal{PT}$ phase diagram and signatures of $\mathcal{PT}$-symmetry breaking in a lattice with PBCs. We have presented a model of a lattice with PBCs and two uniform tunneling amplitudes and shown that the $\mathcal{PT}$-symmetric region for such a model is robust, insensitive to the distance between the loss and gain impurities, and widely tunable in size. We have shown that in such a lattice with PBCs, where there are two different paths from the source to the sink, the motion of a wave packet acquires a chirality when the impurity strength is nonzero. We have predicted that the $\mathcal{PT}$-symmetry breaking in such a lattice is signaled by a universal, maximal value for the steady-state momentum that quantifies this effect. Note that the chirality at an exceptional point – where eigenvalues of a non-Hermitian Hamiltonian become degenerate and corresponding eigenvectors are linearly dependent – has been discussed in the literature [29, 31, 32]. Traditionally, the investigation of signatures of $\mathcal{PT}$-symmetry breaking has focused on the dependence of the intensity profile $I_R(j,t)$, or the net intensity, on time and the impurity strength. These quantities vary smoothly across the phase boundary [30, 33]. In this section, we have shown that the momentum, on the other hand, shows a peak with a universal value at the $\mathcal{PT}$-symmetry-breaking threshold. Such a measurement will require the knowledge of relative phases of the wave function values at adjacent sites, $p(\gamma) \propto \sum_j \mathrm{Im}(f_j^* f_{j+1})$, and therefore is more complex than site-dependent intensity measurements [15,16,19,21,23]. Two-dimensional lattices of coupled waveguides have been experimentally explored [34, 35]. Thus, creating a one-dimensional system with PBCs – a finite (square) lattice with only the boundary waveguides and no interior

waveguides – seems feasible. Our results show that the maximal, universal value of $p(\gamma)$ is achieved at the $\mathcal{PT}$-symmetry-breaking threshold. A deeper understanding of this result and its relation, if any, to the exceptional point [32] remain open questions.

4. BROKEN $\mathcal{PT}$ SYMMETRY IN NONUNIFORM LATTICES

In this chapter, we consider lattice models with a site-dependent ($\mathcal{P}$-symmetric) hopping with both open and periodic boundary conditions, comparing the results in this case with constant-hopping lattices.

4.1 Nonuniform Tunneling Model

In this chapter, we investigate the robustness of the $\mathcal{PT}$-symmetric phase, and the degrees of $\mathcal{PT}$ symmetry breaking in an N-site lattice with a site-dependent hopping function

$$t_\alpha(k) = t_0[k(N-k)]^{\alpha/2} \tag{4.1}$$

and a pair of $\mathcal{PT}$-symmetric impurities $\pm i\gamma$ at positions $(m, \bar{m})$, respectively, where $\bar{m} = N + 1 - m$ is the mirror-symmetric counterpart of site m. With coupled optical waveguides in mind [15,16,23], we explore the signatures of $\mathcal{PT}$ symmetry breaking in the evolution of single-particle properties across the $\mathcal{PT}$-symmetric phase boundary.

We begin with the Hamiltonian for a one-dimensional lattice:

$$H_\alpha = -\sum_{k=1}^{N-1} t_\alpha(k)(a_{k+1}^\dagger a_k + a_k^\dagger a_{k+1}) + i\gamma(a_m^\dagger a_m - a_{\bar{m}}^\dagger a_{\bar{m}}), \tag{4.2}$$

where $a_k^\dagger(a_k)$ is the creation (annihilation) operator for a state localized at site k, and $1 < m < N/2$ is the position of the first impurity. We recall that, for a constant hopping model, as γ/t_0 is increased, the maximum number of complex eigenvalues is given by $2m = 2\mu N \leq N$. This process is always sequential: the number of complex eigenvalues increases by two or four as γ increases; the sole exception is the case with nearest-neighbor impurities, $m = N/2$, where all eigenvalues simultaneously become complex across the $\mathcal{PT}$-symmetric threshold [28]. In the following, we obtain

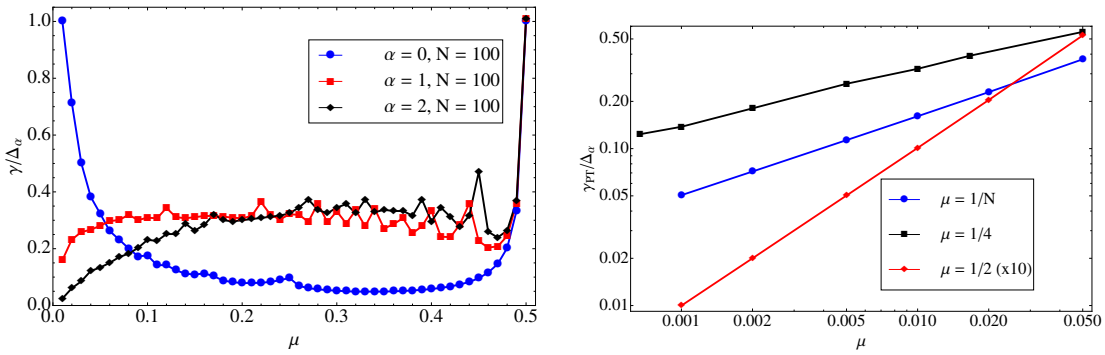

(a) (b)

Fig. 4.1. (a) Typical phase diagram of the Hamiltonian H_α as a function of impurity strength γ/Δ_α and impurity position $\mu = m/N$ for a $N = 100$ site lattice. The region in the $(\gamma/\Delta_\alpha, \mu)$ plane below each curve represents the $\mathcal{PT}$-symmetric phase; it is robust at $\mu = 1/2$. The results are similar for odd N, except that the critical strength when the impurities are closest is $\gamma_{\mathcal{PT}} = \Delta_\alpha/2$. (b) Power-law scaling of $\gamma_{PT}(\mu)/\Delta_\alpha$ vs $1/N$ for an $\alpha = 1$ lattice. Note the logarithmic scale. For farthest impurities ($\mu = 1/N$), $\gamma_{\mathcal{PT}} \sim N^{-1/2}$ (blue). For an intermediate position $\mu = 1/4$, $\gamma_{\mathcal{PT}} \sim N^{-1/3}$ (black). For closest impurities, the approach to the asymptotic limit is the fastest $[\gamma_{\mathcal{PT}}(N) - \gamma_{\mathcal{PT}}(N \to \infty)](\times 10) \sim 1/N$, (red). Thus, the "fragile" phase of an $\alpha > 0$ lattice is significantly stronger than its $\alpha = 0$ counterpart.

α-dependent generalizations of results. When $\alpha > 0$, the bandwidth of a clean lattice scales as $\Delta_\alpha^{'}(N) \sim N^\alpha$; to be consistent with the $\alpha = 0$ case, we use γ/Δ_α as the dimensionless measure of the impurity strength where $\Delta_\alpha = \Delta_\alpha^{'}/4$. The left-hand panel in Fig. 4.1 shows the typical phase diagram for an even lattice ($N = 100$) in the $(\gamma/\Delta_\alpha, \mu)$ plane as a function of the hopping exponent $\alpha \geq 0$. The $\mathcal{PT}$-symmetric threshold, below which all eigenvalues are real, decreases with increasing distance between the impurities, $d = 1 + N(1 - 2\mu)$, but approaches a universal critical values $\gamma_{\mathcal{PT}}/\Delta_\alpha = 1$ when the impurities are the closest, $\mu = 0.5$. When N is odd (not shown), the fragile nature of the $\mathcal{PT}$-symmetric phase is maintained, but the critical strength for closest impurities, $\mu = 0.5(1 - 1/N)$, is reduced by a factor of two,

$\gamma_{\mathcal{PT}} = \Delta_\alpha/2$. In both cases, when $\alpha > 0$, the critical impurity strengths $\gamma_{\mathcal{PT}}(\mu)$ for a generic μ are appreciable compared to their respective universal values at $\mu \approx 1/2$. Thus, the robust nature of the $\mathcal{PT}$-symmetric phase at $\mu = 1/N$ and its extremely fragile nature at generic values of μ are anomalous features of a lattice with constant hopping ($\alpha = 0,$ blue circles) [28].

The right-hand panel in Fig. 4.1 shows typical power-law scaling of the critical impurity strength $\gamma_{\mathcal{PT}}(\mu)$ vs $1/N$ for $\mu = \{1/N, 1/4, 1/2\}$ in a lattice with $\alpha = 1$. When the impurities are farthest, $\mu = 1/N$, the dimensionless critical impurity strength vanishes as $\gamma_{\mathcal{PT}}(N) \sim N^{-1/2}$ (blue circles); when $\mu = 1/4$, it vanishes as $\gamma_{\mathcal{PT}}(N) \sim N^{-1/3}$ (black squares); and when $\mu = 1/2$, it approaches the nonzero critical value as $\gamma_{\mathcal{PT}}(N) - \gamma_{\mathcal{PT}}(N \to \infty) \sim N^{-1}$ (red stars). Note that these results are in stark contrast with the $\alpha = 0$ case where $\gamma_{\mathcal{PT}}(N) \sim N^{-1}$ for all generic μ [28]. Thus, although the $\mathcal{PT}$-symmetric phase of a nonuniform lattice for a generic impurity position is, in principle, algebraically fragile, the critical impurity strength is still appreciably large for experimentally relevant numbers (of waveguides); $\gamma_{\mathcal{PT}}(N)/\Delta_\alpha \sim 0.5 - 0.3$ for $N \leq 100$.

Next, we consider the emergence of complex eigenvalues [36]. For a tight-binding Hamiltonian with a purely imaginary potential, if E is an eigenvalue, then so are $-E$ and E^* [37]. For a given impurity position m, the first (four) complex eigenvalues emerge as two adjacent energy levels $(-E, -E + \delta)$ become degenerate, as do their positive counterparts. Thus, as the fractional impurity position μ changes from the edge of the lattice ($\mu = 1/N$) to its center ($\mu \approx 1/2$), the position of the first complex eigenvalue moves from the center of the energy band, $E = 0$, to its edges, $E \sim \pm 2\Delta_\alpha$. For a given μ, when the impurity strength γ/Δ_α increases, we find that the maximum number of complex eigenvalues is still given by $2\mu N = 2m \leq N$, and that the process is sequential except in an even lattice at $\mu = 1/2$ [28]. Fig. 4.2 shows this generic even-odd effect for the case of closest impurities in a lattice with $\alpha = 2$. For $N = 20, \mu = 0.500$ (red squares), when $\gamma/\Delta_\alpha = 1.08$, just above the even-lattice $\mathcal{PT}$-symmetry-breaking threshold, we see that all N eigenvalues simultaneously become

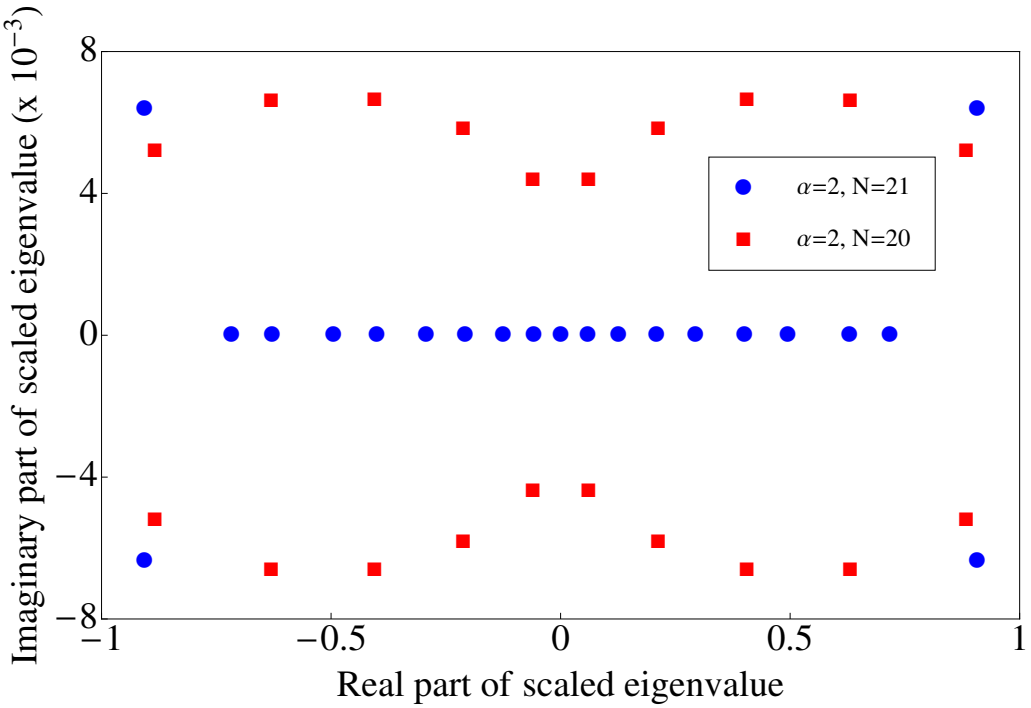

Fig. 4.2. Degrees of $\mathcal{PT}$ symmetry breaking for an $\alpha = 2$ lattice with closest impurities in the odd case ($N = 21, \mu = 0.476$, blue circles) and the even case ($N = 20, \mu = 0.500$, red squares). The complex eigenvalues are scaled by half-bandwidth $2\Delta_\alpha$ and are obtained for impurity strengths just above their respective $\mathcal{PT}$-symmetry-breaking thresholds; $\gamma/\Delta_\alpha = 0.63$ for $N = 21$ and $\gamma/\Delta_\alpha = 1.08$ for $N = 20$. When N is odd (blue circles), we see that four eigenvalues, near the top and the bottom of the energy band, become complex while the remaining $(N - 4)$ remain real; when N is even (red squares), all N eigenvalues simultaneously develop finite imaginary parts. This contrast becomes large for $N \gg 1$.

complex; on the other hand, for $N = 21, \mu = 0.476$ (blue circles), when $\gamma/\Delta_\alpha = 0.63$, just above the odd-lattice $\mathcal{PT}$-symmetry-breaking threshold, four eigenvalues near the band edges become complex and the rest remain real. This difference has dramatic consequences.

4.2 Signatures of $\mathcal{PT}$ Symmetry Breaking

We now explore the signatures of sequential, or simultaneous, $\mathcal{PT}$ symmetry breaking in the time evolution of a single-particle wave packet. It is straightforward to obtain the site- and time-dependent intensity $|\langle k|\psi(t)\rangle|^2$ where $|\psi(t)\rangle = G(t)|\psi(0)\rangle$, and $G(t) = \exp(-iH_\alpha t)$ is the time-evolution operator ($\hbar = 1$) and $|\psi(0)\rangle$ denotes the initial state. We note that since the Hamiltonain H_α is not Hermitian, $G(t)$ is not a unitary operator. With an open (quantum) system in mind, we use the standard inner product to obtain the time-dependent intensity; therefore, the maximum intensity at a site, for a normalized initial state, can exceed unity [38]. Fig. 4.3 shows the evolution of the site- and time-dependent intensity across the $\mathcal{PT}$-symmetric phase boundary for a particle initially localized on the first site shown by the black circle in each panel, $\langle k|\psi(0)\rangle = \delta_{k,1}$, in an $\alpha = 2$ lattice. The vertical axis in each panel represents the site index. The horizontal axes in all panels have the same scale, and represent time in units of $T_\alpha = 1/\Delta_\alpha$. The top two panels show the predicted intensity profile for an odd lattice ($N = 21$) with closest $\mathcal{PT}$-symmetric impurities $\pm i\gamma$, at positions $(10, 12)$. The top panel shows intensity oscillations that occur as the particle bounces from one end of the lattice to the other while encountering the (gain and loss) impurities with strength $\gamma/\Delta_\alpha = 0.626$ at the center. When $\gamma/\Delta_\alpha = 0.627$ (second panel) the $\mathcal{PT}$ symmetry is broken with four complex eigenvalues (see Fig. 4.2). The second panel shows that, over the time-scale shown in Fig. 4.3, the intensity distribution does not change significantly. The bottom two panels are for an even lattice ($N = 20$) with impurities at positions $(10, 11)$. The third panel shows the intensity oscillations that occur in the $\mathcal{PT}$-symmetric phase when $\gamma/\Delta_\alpha = 1.070$. When the impurity strength exceeds the critical value, $\gamma/\Delta_\alpha = 1.074$ (bottom panel), all N eigenvalues become complex, thus maximally breaking the $\mathcal{PT}$ symmetry. This property is manifest in the predicted intensity profile in the bottom panel. Note that we have scaled the color-bar on the bottom two panels to a an identical range to simplify

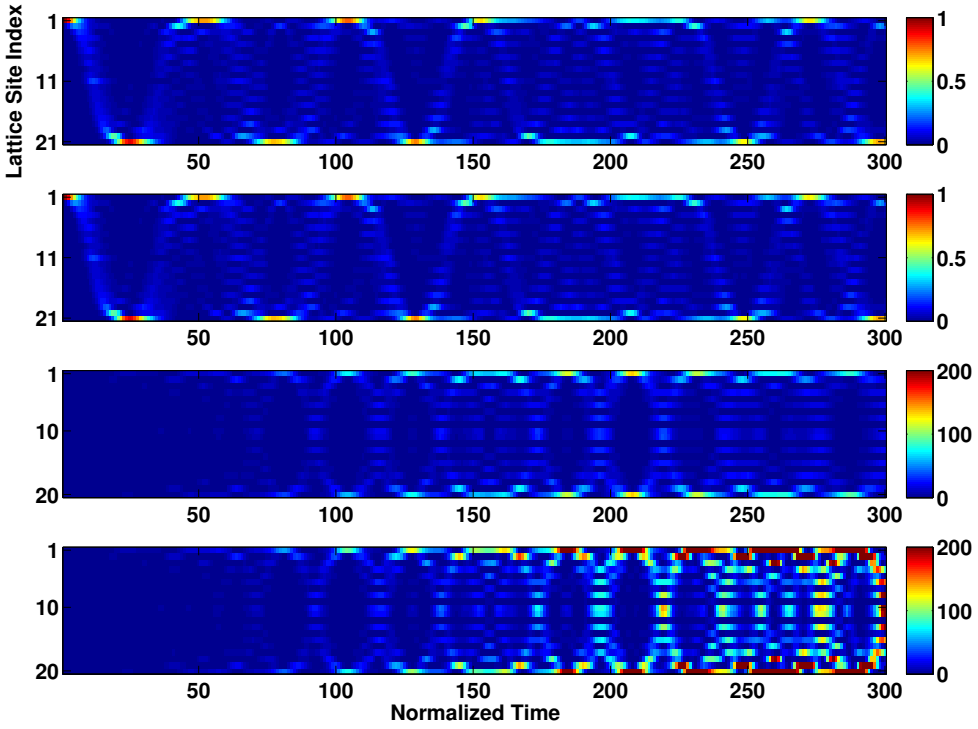

Fig. 4.3. Time evolution of the intensity for a particle initially localized on the first site in an $\alpha = 2$ lattice. The vertical axis in each panel represents the site index, and the horizontal axis represents time in units of $T_\alpha = 1/\Delta_\alpha$. The top two panels are for an odd lattice, $N = 21$, with impurities at sites (10, 12). We see only a small change in the intensity profile as γ/Δ_α is increased from 0.626 (first panel) to 0.627 (second panel). The bottom two panels are for an even lattice, $N = 20$, with impurities at positions (10, 11). We see a marked contrast in the intensity profile when γ/Δ_α is increased from 1.070 (third panel) to 1.074 (fourth panel), when all N eigenvalues become complex.

comparison while maintaing the visibility of structures in the intensity profile; the maximum intensity in the bottom-most panel is $\sim 10^4$.

In this section, we have explored the robustness of the $\mathcal{PT}$-symmetric phase, as well as the degree and signatures of its breaking in a nonuniform lattice with a pair

of imaginary $\mathcal{PT}$-symmetric impurities. We have shown that, when the hopping is maximum near the center of the lattice, $\alpha > 0$, the $\mathcal{PT}$-symmetric phase lasts over an appreciable range of impurity strength and is robust when the impurities are closest to each other. The nature of the $\mathcal{PT}$-symmetry-breaking transition at the robust point in even and odd lattices is different: when $N \gg 1$ is even, all eigenvalues simultaneously become complex, whereas when $N \gg 1$ is odd, only four of the initially do. We have predicted that this difference leads to clear signatures in the intensity profile. In these calculations, we have ignored on-site disorder effects that, in coupled optical waveguides, arise due to variation in the real part of the refractive index. The effect of disorder on the critical impurity strength, as well as the interplay between a disorder that tends to localize the particle to its initial position, and an imaginary potential that tends to localize the particle at the impurity location, will deepen our understanding of these lattice models. Our results suggest that $\mathcal{PT}$ symmetry breaking in a nonuniform lattice with $N \gg 1$ sites will be accompanied by remarkable phonomena, such as the even-odd effect predicted here, with no counterparts in the $N = 2$ system [4].

4.3 Nonuniform Rings

The Hamiltonian for a $\mathcal{PT}$-symmetric ring is given by

$$H(\lambda) = H_\alpha + \lambda_{t_R}\left(a_1^\dagger a_N + a_N^\dagger a_1\right), \tag{4.3}$$

where we choose the tunneling between the end points of the open lattice, sites 1 and N, as $t_R = t_\alpha(1) = t_\alpha(N)$ and the scale-factor $0 \leq \lambda \leq 1$ allows us to continuously extrapolate from an open lattice to a $\mathcal{PT}$-symmetric ring. Before discussing the results for a ring $\lambda > 0$, we briefly recall the results for an open lattice and establish the terminology [33]. In the $\mathcal{PT}$-symmetric phase, the eigenvalue spectrum of an N-site is non-degenerate and symmetric about zero, and the eigenfunctions for energies $\pm\epsilon$ are related to each other. The bandwidth $\Delta_\alpha^{'}$ of the energy spectrum scales as $\Delta_\alpha^{'} \sim N^\alpha$ for $\alpha \geq 0$ and $\Delta_\alpha^{'} \sim N^{-|\alpha|/2}$ for $\alpha < 0$ because the bandwidth is determined

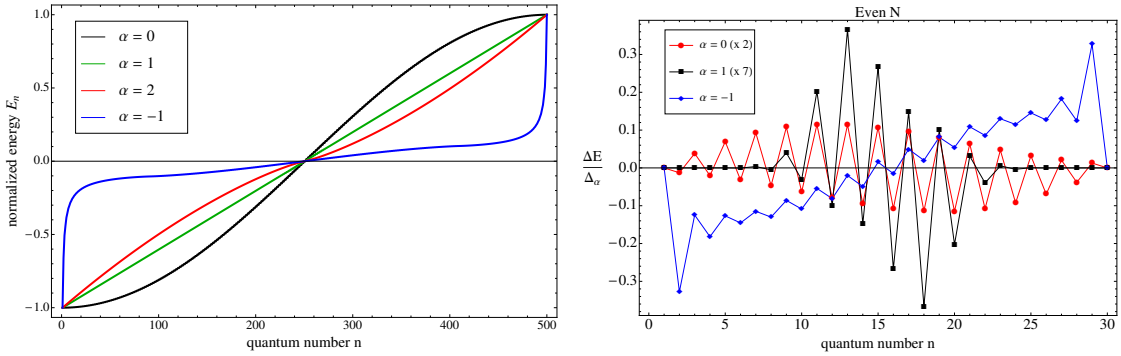

(a) (b)

Fig. 4.4. (a) The energy spectra for a Hamiltonian with $N = 500$ and $\alpha = \{-1, 0, 1, 2\}$, where the energy is normalized by the bandwidth. (b) Shows the difference between energy spectra for a ring and an open lattice for an $N = 30$ lattice. When $\alpha > 0$ the spectral differences are most pronounced near the center of the band. For $\alpha < 0$, the spectral differences are greatest at the band edge and represent the changes that occur in eigenstates localized at the two ends of the open lattice. These results show that the energy spectrum of a $\mathcal{PT}$-symmetric ring is different from that of an open lattice for experimentally relevant lattice sizes.

by the largest tunneling amplitude. We use quarter-bandwidth, $\Delta_\alpha \equiv \Delta_\alpha^{'}/4$ as the energy scale and note that when $\alpha = 0$, the threshold impurity strength is given by $\gamma_{\mathcal{PT}}/\Delta\alpha = 0 = 1$.

Note that although the distinction between an open lattice and a ring is expected to vanish [39] in the limit $N \to \infty$, for small N the differences between the two can be substantial. As an extreme case, let us consider a uniform 3-site lattice with nearest-neighbor tunneling t_0. The non-degenerate, particle-hole symmetric spectrum of such an open lattice is given by $E = \{-\sqrt{2}t_0, 0, \sqrt{2}t_0\}$. On the other hand, the spectrum of a three-site ring is given by $E = \{-2t_0, t_0, t_0\}$ and is, in general, asymmetric about zero and degenerate.

The left-hand panel in Fig. 4.4 shows typical spectra for Hamiltonian (4.3) with $N = 500$ and $\alpha = \{-1, 0, 1, 2\}$. The energy is normalized by its maximum value and since $N \gg 1$, the spectrum is virtually identical for an open lattice and a ring.

When $\alpha = 0$ (black line), we obtain the expected cosine spectrum, for $\alpha = 1$ (green line) and $\alpha = 2$ (red line), the spectrum is quasilinear, and when $\alpha = -1$ (blue line), the spectrum band-edges represent eigenstates localized at the end of the lattice that are generically present when $\alpha < 0$ [40]. The right-hand panel in Fig. 4.4 shows the difference between energies $\Delta E = E_{\text{ring}} - E_{\text{lattice}}$ of a ring and an open lattice for a lattice with $N = 30$ sites and $\alpha = \{-1, 0, 1\}$. We find that for $\alpha > 0$ the difference is greatest near the center of the band, whereas for $\alpha < 0$ the spectral difference is greatest at the band edges. This is expected since the localized edge-states that exist for $\alpha < 0$ are most influenced by the introduction of periodic boundary conditions. The spectral differences vanish with increasing N but remain pertinent for experimentally relevant lattice sizes [19–21].

We now discuss the numerically obtained $\mathcal{PT}$-symmetric phase diagram for the Hamiltonian $H(\lambda)$ as a function of increasing loss and gain impurity strength γ, fractional location of the gain impurity, $\mu = m/N \leq 1/2$, and the dimensionless scale factor λ that extrapolates between an open lattice ($\lambda = 0$) and a ring ($\lambda = 1$). The $\mathcal{PT}$-symmetric phase is called robust if the critical impurity strength measured in units of the energy scale, $\gamma_{\mathcal{PT}}/\Delta_\alpha(N)$ is nonzero as $N \to \infty$; it is called fragile if $\gamma_{\mathcal{PT}}/\Delta_\alpha(N) \to 0$ as $N \to \infty$. In an open lattice $\mu = 1/N$ corresponds to farthest impurities whereas in a ring, farthest impurities correspond to $\mu \sim 1/4$. We note that in an open lattice, when $\alpha > 0$ the critical values of impurity strength $\gamma_{\mathcal{PT}}(\mu)$ decreases as the distance between the impurities increases whereas for $\alpha < 0$, the $\mathcal{PT}$-symmetric phase is vanishingly small for almost all values of impurity location μ [33]. Fig. 4.5 shows the typical evolution of the $\mathcal{PT}$-symmetric phase diagram in the $(\gamma/\Delta_\alpha, \mu)$ plane as a function of the scale parameter λ. These results are for a lattice with $N = 30$ sites, and $\alpha = 1$ (left-hand panel) and $\alpha = 2$ (right-hand panel). For $\lambda = 0$ (black circles), the $\mathcal{PT}$-symmetric phase is robust when the loss and gain impurities are closest to each other, $\mu = 1/2$. Then the critical impurity strength is given by $\gamma_{\mathcal{PT}}/\Delta_\alpha(N) = 1$ when N is even and $\gamma_{\mathcal{PT}}/\Delta_\alpha(N) = 1/2$ when N is odd [33]. For $\lambda > 0$, we see that the critical impurity strength $\gamma_{\mathcal{PT}}$ is, in general, suppressed

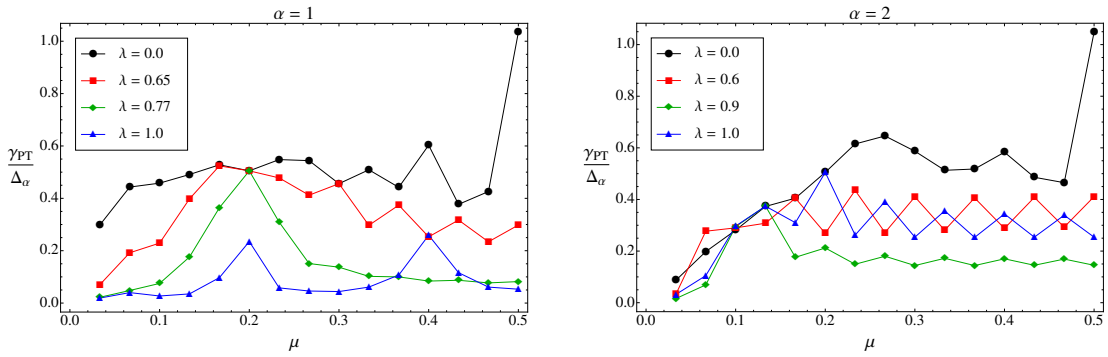

(a) (b)

Fig. 4.5. (a) The $\mathcal{PT}$ phase diagram as a function of impurity strength γ/Δ_α and fractional impurity position $\mu = m/N$ for an $N = 30$-site lattice with $\alpha = 1$. For $\gamma > \gamma_{\mathcal{PT}}$, the eigenvalues of the non-Hermitian Hamiltonian in Eqn. (4.3) become complex. (b) Shows the corresponding results for the $\alpha = 2$ lattice. In both cases, the $\mathcal{PT}$-symmetric phase is maximally robust at $\mu = 1/2$ for an open lattice, $\lambda = 0$ (black circles). As λ is increased, thus increasing the tunneling between sites 1 and N, the critical impurity strength $\gamma_{PT}(\mu)$ remains essentially unchanged from its open lattice value for $\lambda \leq 0.5$. As λ is increased further (red squares, green diamonds), the $\mathcal{PT}$-symmetric phase in the ring ($\lambda = 1$, blue triangles) is weakened for all impurity positions. Thus, a minor change in the Hamiltonian (4.3) leads to a suppression of the critical impurity strength $\gamma_{PT}(\mu)$ even when the impurity location is far away from this change.

relative to its value for an open lattice for all values of impurity positions μ. Thus, the $\mathcal{PT}$-symmetric phase in a ring with non-uniform tunneling is weaker than its counterpart in an open lattice. However, results in Fig. 4.5 also show that the critical impurity strength $\gamma_{\mathcal{PT}}$ is still an appreciable fraction of its value in an open lattice. The left have panel shows that for a lattice with $\alpha = 1$, the critical impurity strength $\gamma_{\mathcal{PT}}(\mu)$ is strongly suppressed except for a few specific values of μ; this feature is robust irrespective of N and is related to the exactly linear spectrum of an $\alpha = 1$ open lattice [38, 41]. The right-hand panel shows that for an $\alpha = 2$ lattice, with a nonlinear spectrum, the critical impurity strength reaches a plateau $\gamma_{\mathcal{PT}}/\Delta_\alpha \sim 0.3$ for most impurity locations $\mu \geq 0.2$. As λ is increased from 0 (red squares, green

diamonds) to 1 (blue triangles) the $\mathcal{PT}$-symmetric Hamiltonian (4.3) is perturbed only slightly. The tunneling introduced between sites 1 and N, $\lambda t_\alpha(1) = \lambda t_\alpha(N)$, is the smallest among all links for $\alpha > 0$. However, it has a dramatic effect on $\gamma_{\mathcal{PT}}$ even when the loss and gain impurities $\pm i\gamma$ are away from this tunneling link, $\mu \geq 0.1$.

When $\alpha < 0$, the tunneling introduced between sites 1 and N is the largest among all links and is proportional to the bandwidth $\Delta_\alpha(N) \sim N^{-|\alpha|/2}$. Therefore, we can expect that the fragile $\mathcal{PT}$-symmetric phase in an open lattice will be strengthened in a ring. Fig. 4.6 shows the $\mathcal{PT}$-symmetric phase diagram for an $N = 30$, $\alpha = -1$ lattice. When $\lambda = 0$ (black circles), we obtain the extremely fragile phase diagram of an open lattice. As the tunneling is increased from $\lambda = 0.2$ (red squares), $\lambda = 0.7$ (green diamonds) to $\lambda = 1.0$ (blue triangles), we see that the $\mathcal{PT}$-symmetric phase in a ring is substantially strengthened for all impurity positions. Since $\mathcal{PT}$-symmetric rings ($\lambda = 1$) with $\alpha > 0$ and $\alpha < 0$ can be mapped onto each other with an appropriate redefinition of the impurity location μ, the critical impurity strength $\gamma_{\mathcal{PT}}(\mu)$ decreases with μ when $\alpha < 0$ (see Fig. 4.6) whereas it increases with μ for $\alpha > 0$ (see Fig. 4.5). We note that in a ring with constant tunneling, accessible to analytical treatment, the critical impurity threshold is zero [42]. These numerical results show that in a ring with non-uniform tunneling $t_\alpha(i)$ there is a large region, below the blue-triangle-curve in Fig. 4.5 and Fig. 4.6, where the $\mathcal{PT}$ symmetry is exact.

4.4 Chirality Across the $\mathcal{PT}$-Symmetric Phase Boundary

The time evolution of a wave packet that is initially localized to a single site has been traditionally used to probe the degrees and signatures of $\mathcal{PT}$ symmetry breaking in coupled optical waveguides [16, 43]. In these systems, the wave function $|\psi(t)\rangle$ denotes the single-transverse-mode electric field in each waveguide [19], the $\mathcal{PT}$-symmetric impurities which absorb or emit the corresponding electromagnetic radiation are engineered, and the time evolution of an initially normalized wave

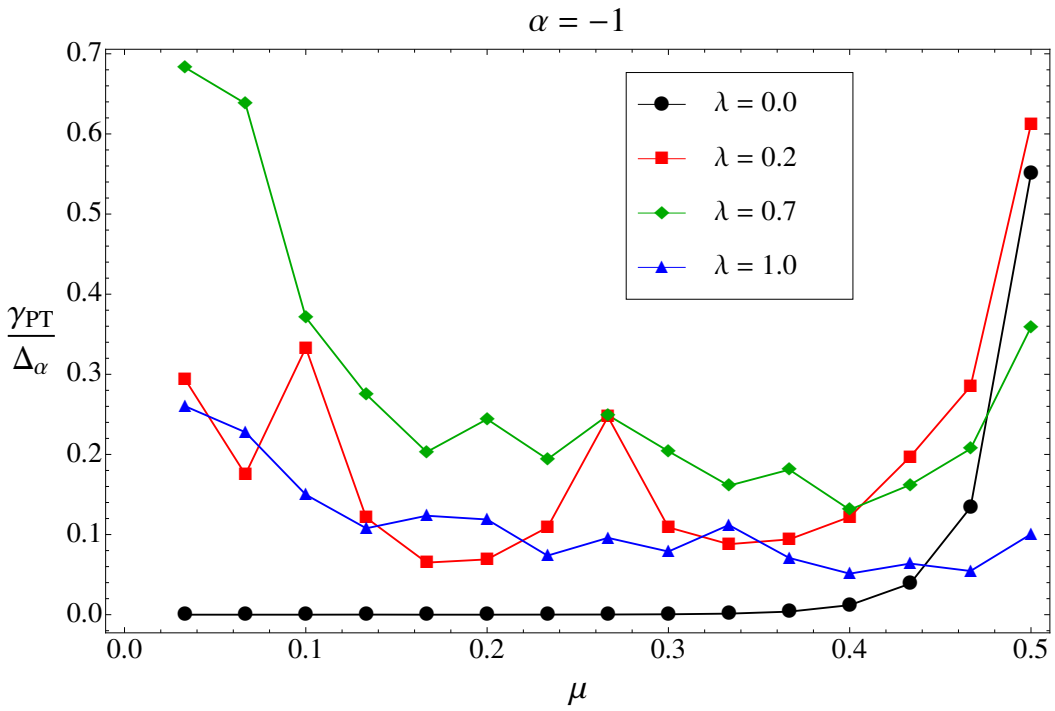

Fig. 4.6. $\mathcal{PT}$-symmetric phase diagram for an $N = 30$ lattice with $\alpha = -1$, as a function of the scale-factor λ that determines the tunneling between sites 1 and N and extrapolates from an open lattice ($\lambda = 0$) to a ring ($\lambda = 1$). When $\lambda = 0$ (black circles), the $\mathcal{PT}$-symmetric phase is fragile everywhere except when the impurities are closest, $\mu = 1/2$. For $\lambda > 0$, the dimensionless critical impurity strength $\gamma_{PT}/\Delta_\alpha$ is significantly enhanced for all impurity locations μ, and, in contrast with the $\alpha > 0$ case, $\gamma_{PT}(\mu)$ for the ring decreases with increasing μ. These results are expected since the tunneling perturbation $\lambda t_\alpha(1)$ scales as the bandwidth for $\alpha < 0$ whereas for $\alpha > 0$, Fig. 4.5, the perturbation scales as $\Delta_\alpha/N^{\alpha/2}$.

packet is given by $|\psi(t)\rangle = \exp(-iH(\lambda)t/\hbar)|\psi(0)\rangle$. The time-evolution operator $\exp(-iH(\lambda)t/\hbar)$ is not unitary irrespective of whether the $\mathcal{PT}$ symmetry is exact or broken; therefore, in general, the net intensity $I(t) = \sum_j I(j,t)$ is not one, where $I(j,t) = |\langle j|\psi(t)\rangle|^2$ denotes the site- and time-dependent intensity. This violation of unitarity is determined by the parity of number of lattice sites N [33], and the localized or extended nature of eigenstates [44]. In all cases, however, the net intensity increases monotonically across and exponentially past the $\mathcal{PT}$-symmetric threshold [30].

The typical time evolution of an initially localized state shows that apart from spreading across different sites, the wave packet undergoes a preferential clockwise or anti-clockwise motion around the ring. As in Chapter 3, we quantify this tendency, chirality, by a dimensionless, Hermitian, discrete-momentum operator on a ring [42],

$$p_\psi(t) = \langle\psi(t)|p|\psi(t)\rangle = -\frac{i\hbar}{2}\sum_{j=1}^{N}\frac{(f_{j+1}^* + f_j^*)(f_{j+1} - f_j)}{|\langle\psi(t)|\psi(t)\rangle|}, \tag{4.4}$$

where $|\psi(t)\rangle = \sum_j f_j(t)|j\rangle$ is a time-evolved wave function, and the normalization factor in the denominator is required due to its non-unitary time evolution. Note that due to the Cauchy-Schwartz inequality, the dimensionless momentum satisfies $-1 \leq p_\psi(t) \leq 1$.

When the Hamiltonian is Hermitian and the initial state is localized to a single site, the momentum $p_\psi(t)$ symmetrically oscillates about zero. As the impurity strength approaches the threshold value, $\gamma \to \gamma_{\mathcal{PT}}(\mu,\alpha)$, $p_\psi(t)$ remains constant over long time intervals $T \sim 100N \gg N$ where the time interval T is measured in units of $2\pi\hbar/\Delta_\alpha$ [33]. We use the time-averaged momentum to denote this steady-state value, $p_\psi(\gamma) = \int_0^T p_\psi(t')dt'/T$, and choose the time interval T such that the steady-state value $p_\psi(\gamma)$ is independent of it.

Fig. 4.7 shows the evolution of the dimensionless momentum $p_\psi(\gamma)$ across the $\mathcal{PT}$-symmetric phase boundary for an $N = 20$ ring with tunneling functions $\alpha = 1$ (left-hand panel) and $\alpha = 2$ (right-hand panel). The initial positions of the wave packet are at $m_0 = 1$ (blue circles dotted line) and $m_0 = 11$ (red squares solid line). Note that when $\mu = m/N = 0.1$, the threshold impurity strength $\gamma_{\mathcal{PT}}(\mu)/\Delta_\alpha$ for $\alpha = 1$

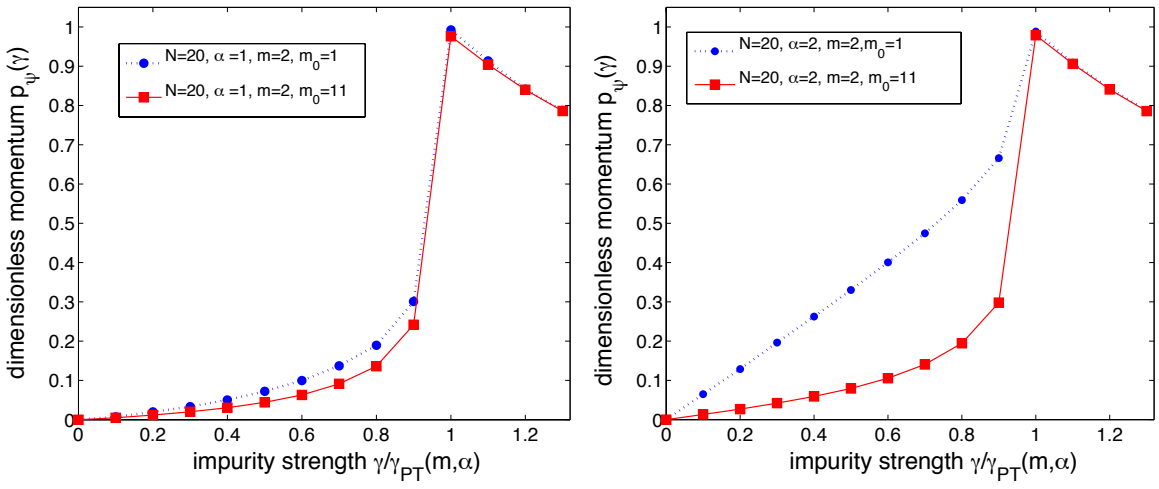

Fig. 4.7. Evolution of the dimensionless, average momentum $p_\psi(\gamma)$ for $N = 20$ lattice with gain impurity $+i\gamma$ at position $m = 2$ ($\mu = 0.1$), and initial wave packet locations $m_0 = 1$ (blue circles dotted line) and $m_0 = 11$ (red squares solid line). The left-hand panel corresponds to tunneling profile with $\alpha = 1$, whereas the right-hand panel has results for $\alpha = 2$. When $\gamma = 0$ the average momentum of the wave packet is zero. For small γ, first-order perturbation theory implies that $p_\psi(\gamma) \propto \gamma$ with a slope that is dependent upon the initial state. In each case, the momentum shows a maximum at the threshold $\gamma = \gamma_{PT}$ and decreases monotonically on both sides of it [42], although the net intensity increases exponentially beyond the threshold [30].

and $\alpha = 2$ differ by an order of magnitude (see Fig. 4.5). In all cases, the average momentum is zero when $\gamma = 0$. Remarkably, in all cases, $p_\psi(\gamma)$ reaches the same maximum possible value (of unity) at the $\mathcal{PT}$-symmetric threshold and decreases monotonically beyond it even though the net intensity $I(t)$ increases exponentially past the threshold.

At this point, it is worthwhile to recall the corresponding results for a $\mathcal{PT}$-symmetric ring with two (constant) tunnelings between the loss and gain impurities. In that case, the threshold strength $\gamma_{\mathcal{PT}}(m)$ is independent of the impurity location m,

the sign of the momentum $p_\psi(\gamma)$ is determined by the path with the higher tunneling amplitude, and it reaches a universal maximum value of one at the threshold [33].

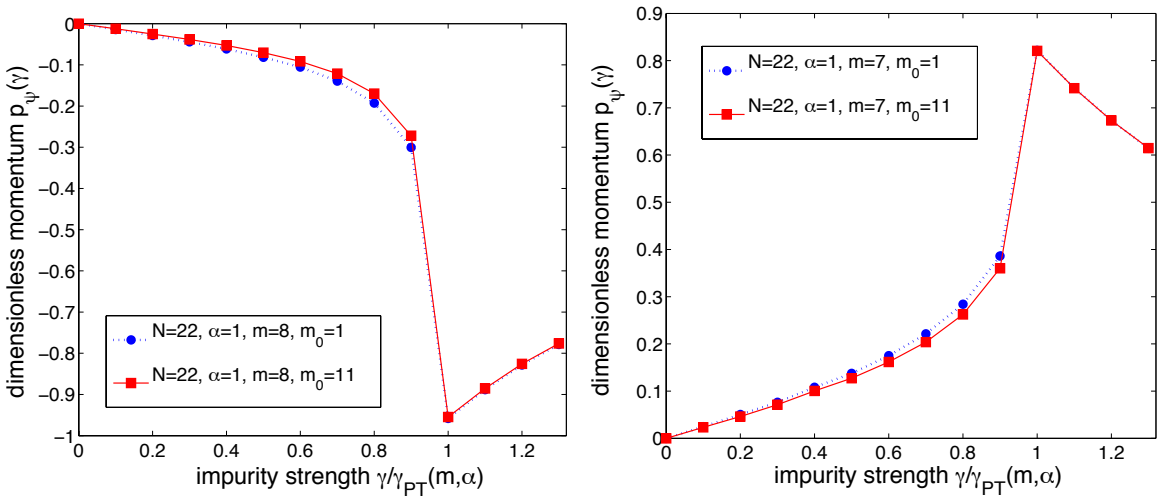

Fig. 4.8. Dimensionless momentum results for an $N = 22$, $\alpha = 1$ ring with initial wave packet at locations $m_0 = 1$ (blue circles dotted line) and $m_0 = 11$ (red squares solid line). The left-hand panel has gain impurity at $m = 8$ ($\mu = 0.364$) whereas the right-panel has gain impurity at location $m = 7$ ($\mu = 0.318$). Due to the position-dependent tunneling Hamiltonian, analytical investigation of momentum dependence on gain impurity location m is not possible. These numerical results show that the sign and the maximum value of the momentum at the threshold are both dependent upon m, but not on the initial wave packet location m_0.

Fig. 4.8 shows that for a ring with non-uniform, position-dependent tunneling profile t_α, the behavior of the steady-state momentum is not as straightforward. Both panels present results for an $N = 22$ ring with $\alpha = 1$ and two initial wave packet locations, $m_0 = 1$ (blue circles dotted line) and $m_0 = 11$ (red squares solid line). The left-hand panel has the gain impurity at location $m = 8$ ($\mu = 0.364$) and it shows that the sign of the steady-state momentum is now negative. The right-hand panel has gain impurity at location $m = 7$ ($\mu = 0.318$) and it shows that the maximum value attained by the steady-state momentum is not-unity. These

results imply that, contrary to the two-tunneling ring, sign of the momentum and the maximum value it attains at the threshold are both dependent upon the impurity location. We emphasize, however, that these results are independent of the initial wave packet location, and the qualitative behavior of $p_\psi(\gamma)$ across the $\mathcal{PT}$-symmetric threshold is identical in all cases.

4.5 Conclusions

In this section, we have numerically explored the $\mathcal{PT}$-symmetric phase diagram for a finite, nonuniform $\mathcal{PT}$-symmetric lattice as a function of its boundary conditions. We have shown that for experimentally relevant lattice sizes, the differences between properties of an open lattice and a ring are nontrivial, particularly for tunneling profiles $t_\alpha(k)$ with $\alpha < 0$. Generically, we found that for $\alpha > 0$, the $\mathcal{PT}$-symmetric phase is a ring is weaker than its counterpart in an open lattice. In contrast, when $\alpha < 0$ the $\mathcal{PT}$-symmetric phase in a ring is substantially strengthened. Since for $\alpha < 0$ the tunneling perturbation that is required to change an open lattice into a ring is comparable to the bandwidth of the open lattice, the strengthening of the $\mathcal{PT}$-symmetric phase is reasonable.

We have shown that the $\mathcal{PT}$ symmetry breaking is accompanied by a qualitatively universal behavior of dimensionless, average momentum $p_\psi(\gamma)$: the momentum is zero when $\gamma = 0$, increases linearly with γ, and its magnitude reaches a maximum at the $\mathcal{PT}$ breaking threshold, accompanied by monotonic decay on both sides of the threshold. We have also found that, in contrast with the two-tunneling model [42], here, the sign of the momentum and its maximum value at the threshold are dependent upon the impurity locations, but not on the initial wave packet location.

These numerical results raise several questions. For an open lattice, the location of the pair of eigenvalues that become degenerate and then complex is uniquely determined by the impurity location μ irrespective of the value of α [33]; no such claim seems possible for the $\mathcal{PT}$ symmetry breaking in a ring. The universal presence of

the peak in $|p_\psi(\gamma)|$ at the threshold $\gamma = \gamma_{\mathcal{PT}}(\mu, \alpha)$ suggests that it may be driven by the exceptional point at the threshold where two eigenvalues become degenerate and the corresponding eigenvectors become parallel [32]. However, lacking analytical methods for the non-uniform tunneling ring, a systematic numerical investigation of the dependence of the sign and the maximum value of the chirality remains an open problem. In the next chapter, we will study the effects of competing $\mathcal{PT}$ potentials on a lattice and compare the results to their counterparts in the continuum limit.

5. COMPETING $\mathcal{PT}$ POTENTIALS ON A LATTICE

In this Chapter we explore the effects of competition between localized and extended $\mathcal{PT}$ potentials on a lattice. Our starting point, as before, is the one-dimensional, tight-binding chain having N lattice sites, site-to-site distance a, and a tunneling $t_0 > 0$ between adjacent sites under open boundary conditions. Again, the Hermitian tunneling Hamiltonian is given by

$$H_0 = -t_0 \sum_{i=1}^{N-1} \left(a_{i+1}^\dagger a_i + a_i^\dagger a_{i+1} \right), \tag{5.1}$$

The localized potentials take the form of two on-site impurities $(+i\gamma, -i\gamma)$ located at mirror-symmetric positions $(m, \bar{m})$, where $\bar{m} = N + 1 - m$. The short-range impurity potential term, then, is given by

$$V = i\gamma \left(a_m^\dagger a_m - a_{\bar{m}}^\dagger a_{\bar{m}} \right). \tag{5.2}$$

The $\mathcal{PT}$ phase digram for localized potentials on a lattice has been extensively explored [24, 26, 28]. One of the salient features of this system is that the position of the localized impurities along the lattice allows for tunability in where the $\mathcal{PT}$ breaking occurs in the energy band. When the impurities are closest the eigenvalues at the outermost band edges become degenerate, indicating the the $\mathcal{PT}$ symmetry has been broken. Alternatively, when the impurities are maximally separated, the $\mathcal{PT}$ breaking occurs at the center of the band.

The extended potential takes the form of a series of $\mathcal{PT}$-symmetric on-site potentials with amplitudes prescribed by

$$V_\alpha(k) = i\gamma \mathrm{sgn}(k - N_c)|k - N_c|^\alpha a_k^\dagger a_k, \tag{5.3}$$

where $N_c = (N+1)/2$ is the central lattice site, and there is only a site at the center for odd N. We numerically determine that the $\mathcal{PT}$-symmetric threshold $\gamma_{\mathcal{PT}}(\alpha, N)$,

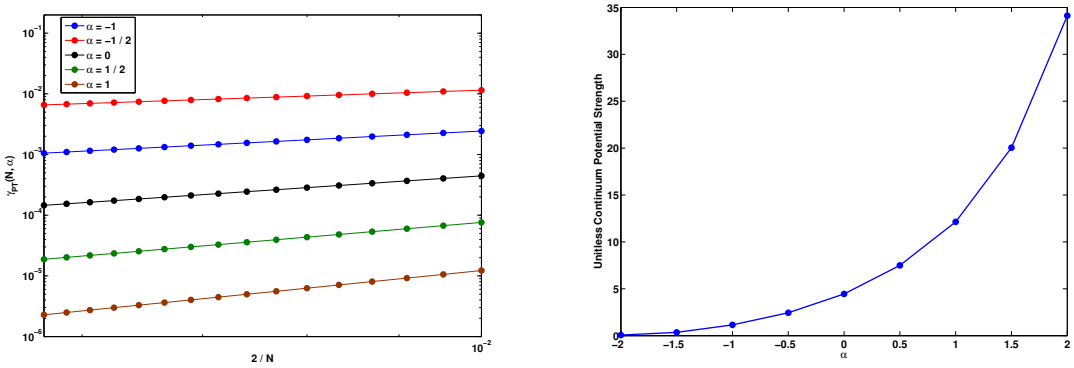

(a) (b)

Fig. 5.1. (a) Dependence of the threshold $\gamma_{\mathcal{PT}}(\alpha, N)$ on the potential exponent α and the lattice size N. Note the logarithmic scale. (b) Unitless continuum potential strength vs α. The results are consistent with those determined by Znojil [45] for $\alpha = 0$ (~ 4.48) and Serbyn [46] for $\alpha = 1$ (~ 12.31).

below which all eigenvalues of the Hamiltonian are purely real, decreases with increasing N and α according to the expression

$$\gamma_{\mathcal{PT}}(\alpha, N) = \Gamma_\alpha \left(\frac{2}{N}\right)^{\alpha+2}, \tag{5.4}$$

where Γ_α is closely related to the $\mathcal{PT}$-symmetric threshold in the continuum counterpart to the lattice.

5.1 Continuum Limit Considerations

We now compare the lattice case to its counterpart in the continuum limit, namely a line with $-L \leq x \leq L$. So we have $N \to \infty$, $a \to 0$ such that the product $Na = 2L$ remains finite; likewise, the lattice site index k goes over to the continuum position $x = (k - n_c)a$, which ranges from $-L \leq x \leq L$ for $1 \leq k \leq N$. We recall that a particle hopping on a tight-binding lattice, with band structure $E_k = -2J\cos(2\pi k/(N+1))$, translates into a particle with effective mass m given by $\hbar^2/2m = \lim_{a\to 0} Ja^2$. The potential in Eqn. (5.3) becomes, in the thermodynamic limit, $V_\alpha(x) = i\bar{\Gamma}\mathrm{sgn}(x)|x|^\alpha$, where $|x| \leq L$ and $\bar{\Gamma} = \lim_{a\to 0} \gamma/a^\alpha$ has units of Energy / Length$^\alpha$.

When $\alpha = 2n + 1$, the Schrödinger equation with the $\mathcal{PT}$ potential becomes

$$-\frac{\hbar^2}{2m}\partial_x^2\psi_q(x) + i\bar{\Gamma}x^\alpha\psi_q(x) = E_q\psi_q(x) \tag{5.5}$$

with the boundary conditions $\psi_q(\pm L) = 0$. When comparing the lattice and continuum potentials (γ and $\bar{\Gamma}$, respectively), we see that $\gamma/(\hbar^2/2m) = \bar{\Gamma}(2/N)^{(\alpha+2)}$. Since $\gamma_{\mathcal{PT}}$ scales as $(2/N)^{\alpha+2}$, this implies that the $\mathcal{PT}$-symmetric threshold in the continuum limit $\bar{\Gamma}_{\mathcal{PT}}$ remains finite. This finite threshold has been calculated for the $\alpha = 0$ case [45] and the $\alpha = 1$ case [46], and the results are consistent with those calculated numerically in Fig. 5.1(b).

5.2 Competing $\mathcal{PT}$ Potentials

We now investigate how competition between the two localized $\mathcal{PT}$ impurities and the extended $\mathcal{PT}$ potentials on the lattice affects the $\mathcal{PT}$ phase diagram. We

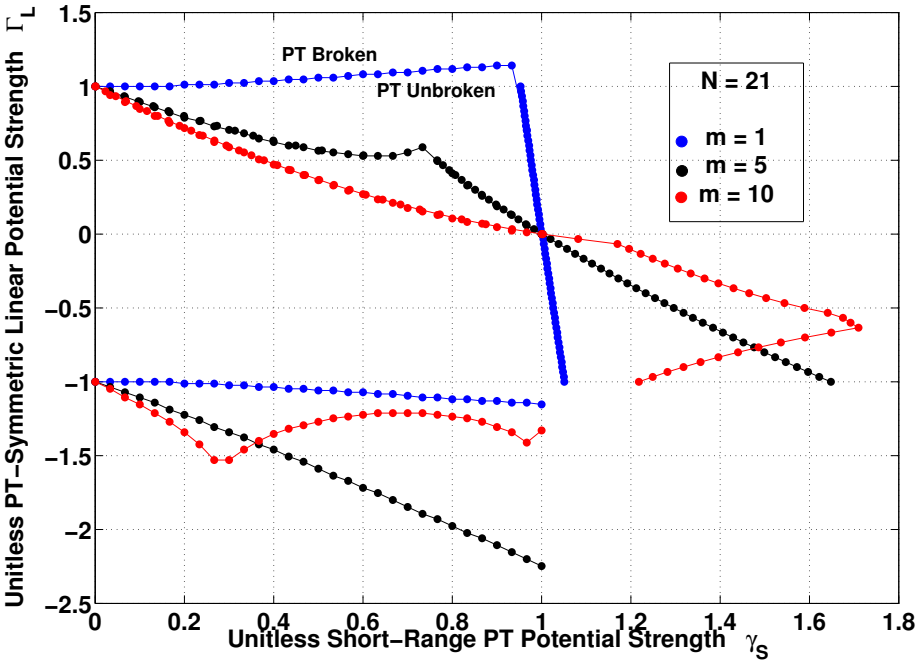

Fig. 5.2. $\mathcal{PT}$ phase diagram for a $N = 21$-site lattice with two localized $\mathcal{PT}$ potentials located at parity-symmetric positions in the presence of an extended linear potential. When the short-range impurities are the closest, we recover the naive expectation of two parallel lines. When the impurities are the farthest, however, we see a re-entrant phase behavior.

begin by considering the linear $\mathcal{PT}$ potential in the presence of two localized $\mathcal{PT}$ potentials. Fig. 5.2 shows the $\mathcal{PT}$ phase diagram for a $N = 21$-site lattice with two localized $\mathcal{PT}$ potentials located at parity-symmetric positions in the presence of an extended linear ($\alpha = 1$) $\mathcal{PT}$ potential. The vertical axis represents the critical linear potential strength Γ_L (in units of the critical strength in the absence of the two localized potentials) while the horizontal axis denotes the critical short-range impurity strength γ_S (also in units of the critical strength in the absence of the linear potential). The naïve expectation for the phase diagram would be the direct sum of the linear and localized potentials ($\gamma_{\mathcal{PT}} = \gamma_S + \Gamma_L$) which is in good agreement with what is found in the case when the localized impurities are the closest ($m = 10, \text{red dots}$). As we move the localized impurities farther apart on the lattice, we begin to see a deviation from this behavior ($m = 5, \text{black dots}$) especially in the first and third quadrants. Remarkably, when the short-range potentials are maximally separated on the lattice we see a dramatically different behavior ($m = 1, \text{blue dots}$). This robust $\mathcal{PT}$ phase suggests that it is possible to transition continuously from a region of broken $\mathcal{PT}$ symmetry to a region of unbroken $\mathcal{PT}$ symmetry by increasing the localized loss in the broad loss region. To illustrate that this is a generic phenomenon, Fig. 5.3 shows similar $\mathcal{PT}$ phase diagrams for different values of α which also exhibit a robust $\mathcal{PT}$-symmetric phase when the localized impurities are maximally separated.

5.3 Wave Packet Dynamics

We have shown previously that, for a fixed value of the linear potential strength Γ_L, we can move continuously along the $\mathcal{PT}$ phase diagram from a region of broken $\mathcal{PT}$ symmetry to a region of unbroken $\mathcal{PT}$ symmetry by tuning the strength of the two on-site $\mathcal{PT}$ potentials. We now explore the effects of this $\mathcal{PT}$ phase transition on the time-evolution of a single-particle wave packet on the lattice. For an initial state $|\psi(0)\rangle$, the time-evolved state is given by $|\psi(t)\rangle = G(t)|\psi(0)\rangle$, where $G(t) = \exp[-iHt/\hbar]$ is determined numerically.

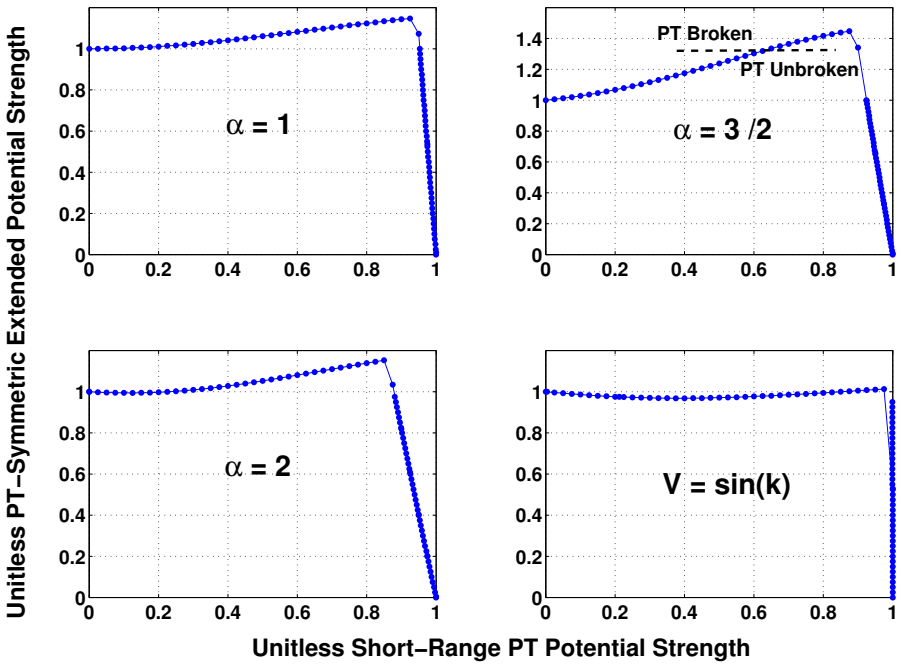

Fig. 5.3. $\mathcal{PT}$ phase diagrams for a $N = 21$-site lattice with two localized $\mathcal{PT}$ potentials located at parity-symmetric positions in the presence of an extended potential for different values of the exponent α. We see that the re-entrant phase behavior is a generic phenomenon.

Figure 5.4 shows the site- and time-dependent intensity profile for a particle initially localized on the first site of a $N = 21$ lattice with competing short-range and linear potentials. The vertical axis in each panel represents the site index, while the horizontal axis denotes normalized time. In each panel, the short-range loss (gain) is located on site $m = 1$ ($m = 21$), and the loss end of the linear potential begins at site $m = 1$ and increases through site $m = 21$. For the top panel, the linear potential strength $\Gamma_L = 1.05\Gamma_{L_{\mathcal{PT}}}$ while the short-range impurity strength $\gamma_S = 0.25\gamma_{S_{\mathcal{PT}}}$. Since the $\mathcal{PT}$ symmetry is broken in this region (shown in figure 5.2), we see the exponential growth in intensity due to the emergence of complex eigenvalues. In the bottom panel, the linear potential strength remains fixed at $\Gamma_L = 1.05\Gamma_{L_{\mathcal{PT}}}$, while the short-range impurity strength is increased to $\gamma_S = 0.75\gamma_{S_{\mathcal{PT}}}$. Now that we have

transitioned to a region of unbroken $\mathcal{PT}$ symmetry, we no longer see an exponential growth in intensity since the spectrum is entirely real.

We conclude this chapter by investigating the case of two competing extended sinusoidal potentials on the lattice. The potential term in the Hamiltonian is now of the form

$$V_\alpha(k) = \{i\gamma_1 \sin[2\pi\beta_1(k - N_c)] + i\gamma_2 \sin[2\pi\beta_2(k - N_c)]\}\, a_k^\dagger a_k, \tag{5.6}$$

where $0 \leq \beta_1, \beta_2 \leq 1$. Fig. 5.5(a) shows the $\mathcal{PT}$ phase diagram in the (γ_1, γ_2) plane for a $N = 40$ lattice. We see even in the case of two competing sinusoidal potentials, the re-entrant $\mathcal{PT}$ phase is still present, indicating that re-entrant phase is truly a generic phenomenon. Fig. 5.5(b) shows the time evolution of a wave packet initially localized at site $m_0 = 1$. The top panel gives the time evolution for $\gamma_1 = 0.4\gamma_{1\mathcal{PT}}$

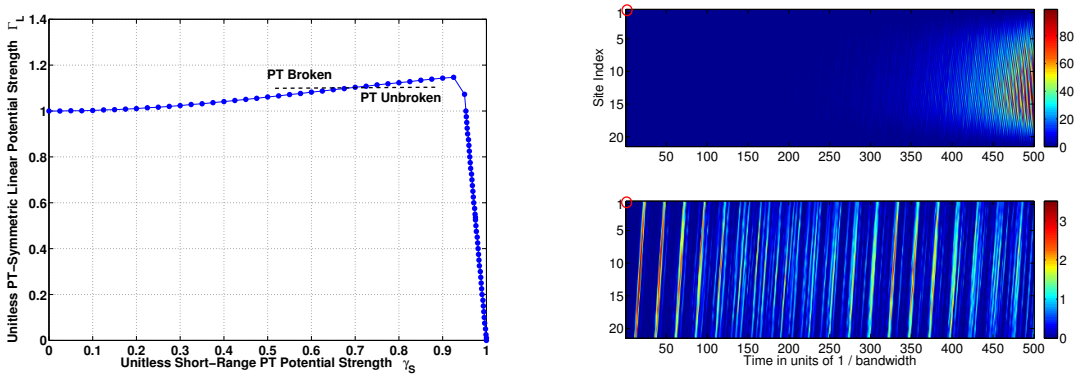

(a) (b)

Fig. 5.4. (a) $\mathcal{PT}$ phase diagram for a $N = 21$ lattice with an extended linear ($\alpha = 1$) potential and two localized potentials. We see that it is possible to transition from a region of broken $\mathcal{PT}$ symmetry to a region of unbroken $\mathcal{PT}$ symmetry by increasing the strength of the localized loss. (b) Site- and time- dependent intensity profile for a single-particle wave packet traveling along the lattice. The top panel shows the exponential increase in the intensity due to a broken $\mathcal{PT}$ symmetry. In the bottom panel, the $\mathcal{PT}$ symmetry is restored by moving horizontally along the phase diagram in (a).

and $\gamma_2 = 1.044\gamma_{2\mathcal{PT}}$ in a region of broken $\mathcal{PT}$ symmetry. As expected, the intensity diverges exponentially with time. Moving horizontally on the $\mathcal{PT}$ phase diagram along the line $\gamma_2 = 1.044\gamma_{2\mathcal{PT}}$, we arrive at the point $\gamma_1 = 0.8\gamma_{1\mathcal{PT}}$ in a region of unbroken $\mathcal{PT}$ symmetry – reflected by the bottom panel in Fig. 5.5(b).

5.4 Conclusions

In this chapter, we have explored the competition between localized and extended $\mathcal{PT}$ potentials on a lattice. We found that the fragile $\mathcal{PT}$ phase for the extended potential in lattice case translated to a finite $\mathcal{PT}$ threshold in the continuum limit. The most surprising result was from the phase diagram for the competing potentials. We determined that an increase in strength of the short-range $\mathcal{PT}$ impurities resulted

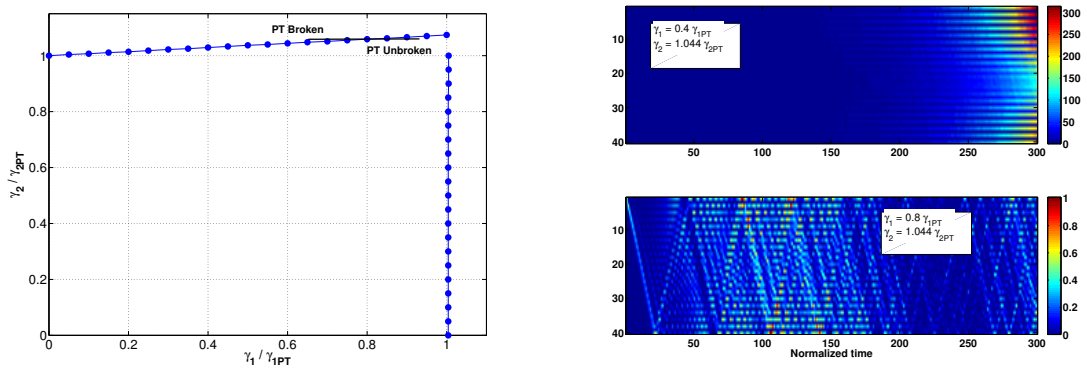

(a) (b)

Fig. 5.5. (a) $\mathcal{PT}$ phase diagram for a $N = 40$ lattice with competing sinusoidal potentials. We again see that it is possible to transition from a region of broken $\mathcal{PT}$ symmetry to a region of unbroken $\mathcal{PT}$ symmetry by increasing the strength of one of the sinusoidal potentials. (b) Site- and time- dependent intensity profile for a single-particle wave packet traveling along the lattice. The top panel shows the exponential increase in the intensity due to a broken $\mathcal{PT}$ symmetry. In the bottom panel, the $\mathcal{PT}$ symmetry is restored by moving horizontally along the phase diagram in (a).

in a re-entrant $\mathcal{PT}$ phase. That is, increasing localized loss in the broad-loss region actually served to restore the broken $\mathcal{PT}$ symmetry. This effect had significant consequences for the dynamics of a single-particle wave packet. The re-entrant phase meant that it was possible to transition between a region of broken $\mathcal{PT}$ symmetry to a region of unbroken $\mathcal{PT}$ symmetry, as evidenced by the change from an exponentially increasing wave packet intensity to a steady intensity.

6. SUMMARY

In this thesis, we have investigated the consequences of $\mathcal{PT}$ symmetry breaking in tight-binding lattice systems. In Chapter 2, we explored the $\mathcal{PT}$ phase diagram for an N-site lattice with uniform Hermitian tunneling in the presence of two on-site $\mathcal{PT}-$symmetric impurities. We found that the $\mathcal{PT}$ phase was robust for the case of either closest or farthest impurities (with open boundary conditions) and fragile elsewhere. Also, we calculated the change in a typical dimensionless eigenfunction as a function of the impurity potential γ in the case of nearest-neighbor impurities across the $\mathcal{PT}$ phase boundary. We found that a spontaneously broken $\mathcal{PT}$ symmetry is manifest in the asymmetrical wave function amplitude.

In Chapter 3 we numerically investigated the $\mathcal{PT}$ phase diagram for a lattice with periodic boundary conditions and uniform tunneling. For a $\mathcal{PT}$-symmetric ring with two tunnelings, the $\mathcal{PT}$ phase was found to be robust irrespective of the impurity locations on the ring. We have also shown that in a ring, where there are two paths from the source to the sink, the motion of a wave packet acquires a chirality when the impurity strength is nonzero. We quantified this effect via a discrete momentum operator and found a maximal value for the steady-state momentum.

In Chapter 4, we explored the signatures of broken $\mathcal{PT}$ symmetry in lattices with nonuniform tunneling profiles. We demonstrated that for experimentally relevant lattice sizes, the differences between an open chain and a ring are significant. Specifically, we found that for $\alpha > 0$, the $\mathcal{PT}$-symmetric phase in a ring is weaker than its counterpart in a lattice with open boundary conditions. Moreover, we found that, in contrast with the two-tunneling model in Chapter 2, the sign of the momentum and its maximum value at the $\mathcal{PT}$ threshold are dependent upon the impurity locations, but not on the initial wave packet location.

Finally, we examined the competition between localized and extended $\mathcal{PT}$ potentials on a lattice. In the case where the localized potentials were the farthest, we found a remarkable re-entrant $\mathcal{PT}$-symmetric phase. This indicated that the addition of localized loss to a broad-loss region actually served to strengthen the $\mathcal{PT}$ phase. This re-entrant phase also has dramatic consequences on the time evolution of a wave packet. The re-entrant phase meant that it was possible to transition between a region of broken $\mathcal{PT}$ symmetry to a region of unbroken $\mathcal{PT}$ symmetry, as evidenced by the change from an exponentially increasing wave packet intensity to a steady intensity.

In summary, there is a great deal of rich physics to be explored in the field of $\mathcal{PT}$ symmetry. It is truly remarkable how broadly applicable effective $\mathcal{PT}$ Hamiltonians are to describing the dynamics of a diverse range of systems. We would like to briefly mention, however, the potential challenges of describing $\mathcal{PT}$-symmetric systems in terms of equilibrium statistical mechanics and the resulting counterintuitive implications. The partition function $Z(\beta) = \sum_n e^{-\beta E_n}$, where $\beta = 1/kT$, is a monotonically decreasing function of β for the systems traditionally dealt with in statistical mechanics. This monotonic behavior implies that the thermodynamic quantities derived from the partition function (e.g. specific heat) will also exhibit a monotonic behavior in temperature. For instance, we expect that as we continually add energy to a system in, say, the solid phase, it will transition to the liquid and gas phases with increasing temperature. This raises some interesting questions for $\mathcal{PT}$-symmetric systems which are inherently not in equilibrium, particularly above the $\mathcal{PT}$ phase boundary. As shown previously, at the $\mathcal{PT}$ phase boundary the energy spectrum becomes complex, implying that partition function will begin to exhibit an oscillatory behavior. This would mean that, in the case of the specific heat, we could continually increase the temperature of the system, yet perpetually oscillate between two phases. Results such as this do not resonate with our physical intuition, so it raises important questions as to whether or not $\mathcal{PT}$-symmetric systems can be adequately treated by equilibrium statistical mechanics.

This thesis has dealt exclusively with one-dimensional $\mathcal{PT}$ lattices described by the (linear) Schrödinger equation. One avenue of future interest would be to examine nonlinear effects on the dynamics of wave packet behavior on the lattice. These nonlinear effects would become especially relevant at the $\mathcal{PT}$-symmetry-breaking threshold and beyond when the wave packet intensity increases exponentially. Due to its formal equivalence to the paraxial diffraction equation for light in a waveguide [16], we believe that the nonlinear Schrödinger equation (NLSE),

$$i\frac{\partial\psi}{\partial t} + P\frac{\partial^2\psi}{\partial x^2} + Q\psi + R|\psi|^2\psi = 0, \tag{6.1}$$

would be a prime candidate for exploring nonlinear behavior. The coefficients P, Q, and R depend upon the particular problem of interest, as do the physical meanings of the variables t and x. While prohibitive to analytical treatment, the NLSE can certainly allow us to calculate the time evolution of the system; given the state $\psi(t_0)$, we can use Eqn. (6.1) to determine the state at a later time $\psi(t_0 + \epsilon)$ and therefore iteratively determine the state $\psi(t)$ at all later times t. Soliton solutions to Eq. (6.1) are of particular interest. A soliton is a solitary wave, localized in spatial extent, with remarkable stability properties. Solitons are intrinsically nonlinear phenomena that derive their stability from a delicate balance of competing dispersive and nonlinear influences. Soliton solutions are ubiquitous in physics, appearing in the Korteweg-de Vries equation for shallow water waves, electrical lines, fiber optics, blood pressure waves, coupled pendulua, and a host of other diverse areas [47]. Intriguing questions arise as to the existence of solitonic solutions to Eqn. (6.1) but with the addition of $\mathcal{PT}$-symmetric impurities. If they do exist, what would their interaction look like on the lattice? By answering these questions, further insight could be gained into how and when $\mathcal{PT}$-symmetric Hamiltonians can be used to effectively model various systems in condensed matter physics.

LIST OF REFERENCES

LIST OF REFERENCES

[1] P. Dirac, *The Principles of Quantum Mechanics*. New York: Oxford University Press, 1996.

[2] P. Dennery and A. Krzywicki, *Mathematics for Physicists*. Mineola, NY: Dover Publications, 1995.

[3] J. J. Sakurai, *Modern Quantum Mechanics*. Reading, MA: Addison-Wesley, 1995.

[4] C. M. Bender and S. Boettcher, "Real Spectra in Non-Hermitian Hamiltonians Having $\mathcal{PT}$ Symmetry," *Phys. Rev. Lett.*, vol. **80**, pp. 5243–5246, Jun 1998.

[5] C. M. Bender, D. C. Brody, and H. F. Jones, "Complex Extension of Quantum Mechanics," *Phys. Rev. Lett.*, vol. **89**, p. 270401, Dec 2002.

[6] A. Mostafazadeh, "Pseudo-Hermiticity versus $\mathcal{PT}$ Symmetry: the Necessary Condition for the Reality of the Spectrum of a Non-Hermitian Hamiltonian," *J. Math. Phys.*, vol. **43**, p. 205, 2002.

[7] A. Mostafazadeh, "Exact $\mathcal{PT}$-symmetry is equivalent to Hermiticity," *J. Phys. A: Math. Theor.*, vol. **36**, no. 25, p. 7081, 2003.

[8] A. Mostafazadeh, "Quantum Brachistochrone Problem and the Geometry of the State Space in Pseudo-Hermitian Quantum Mechanics," *Phys. Rev. L*, vol. **99**, no. 13, p. 130502, 2007.

[9] M. Znojil, "Gegenbauer-solvable quantum chain model," *Phys. Rev. A*, vol. **82**, no. 5, p. 052113, 2010.

[10] M. Znojil, "Tridiagonal $\mathcal{PT}$-symmetric N -by- N Hamiltonians and a fine-tuning of their observability domains in the strongly non-Hermitian regime," *Jour. Phys. A: Math. Theor.*, vol. **40**, no. 43, p. 13131, 2007.

[11] M. Znojil, "Conditional observability," *Phys. Lett. B*, vol. **650**, no. 56, pp. 440 – 446, 2007.

[12] X. G. Wen, *Quantum Field Theory of Many-Body Systems*. Oxford University Press: New York, 2004.

[13] I. Bloch, "Ultracold Quantum Gases in Optical Lattices," *Nat. Phys.*, vol. **1**, no. 1, pp. 23–30, 2005.

[14] D. Jaksch and P. Zoller, "The Cold Atom Hubbard Toolbox," *Ann. Phys.*, vol. **315**, no. 1, pp. 52–79, 2005.

[15] A. Guo, G. J. Salamo, D. Duchesne, R. Morandotti, M. Volatier-Ravat, V. Aimez, G. A. Siviloglou, and D. N. Christodoulides, "Observation of $\mathcal{PT}$-Symmetry Breaking in Complex Optical Potentials," *Phys. Rev. Lett.*, vol. **103**, p. 093902, Aug 2009.

[16] C. E. Ruter, K. G. Makris, R. El-Ganainy, D. N. Christodoulides, and M. Segev, "Observation of parity-time symmetry in optics," *Nat. Phys.*, vol. **6**, pp. 192–195, 2010.

[17] A. Regensburger, C. Bersch, M.-A. Miri, G. Onishchukov, D. N. Christodoulides, and U. Peschel, "Parity-time synthetic photonic lattices," *Nature*, vol. **488**, no. 7410, pp. 167–171, 2012.

[18] J. Schindler, A. Li, M. C. Zheng, F. Ellis, and T. Kottos, "Experimental study of active LRC circuits with $\mathcal{PT}$ symmetries," *Phys. Rev. A*, vol. **84**, no. 4, p. 040101, 2011.

[19] D. N. Christodoulides, F. Lederer, and Y. Silberberg, "Discretizing Light Behaviour in Linear and Nonlinear Waveguide Lattices," *Nature*, vol. **424**, pp. 817–823, 2003.

[20] A. Perez-Leija, H. Moya-Cessa, A. Szameit, and D. N. Christodoulides, "Glauber–Fock photonic lattices," *Opt. Lett.*, vol. **35**, pp. 2409–2411, Jul 2010.

[21] Y. Lahini, A. Avidan, F. Pozzi, M. Sorel, R. Morandotti, D. N. Christodoulides, and Y. Silberberg, "Anderson Localization and Nonlinearity in One-Dimensional Disordered Photonic Lattices," *Phys. Rev. Lett.*, vol. **100**, p. 013906, Jan 2008.

[22] K. G. Makris, R. El-Ganainy, D. N. Christodoulides, and Z. H. Musslimani, "Beam Dynamics in $\mathcal{PT}$-Symmetric Optical Lattices," *Phys. Rev. Lett.*, vol. **100**, p. 103904, Mar 2008.

[23] T. Kottos, "Optical Physics: Broken Symmetry Makes Light Work," *Nat. Phys.*, vol. **6**, pp. 166–167, 2010.

[24] L. Jin and Z. Song, "Solutions of $\mathcal{PT}$-Symmetric Tight-Binding Chain and its Equivalent Hermitian Counterpart," *Phys. Rev. A*, vol. **80**, p. 052107, Nov 2009.

[25] O. Bendix, R. Fleischmann, T. Kottos, and B. Shapiro, "Exponentially Fragile $\mathcal{PT}$ Symmetry in Lattices with Localized Eigenmodes," *Phys. Rev. Lett.*, vol. **103**, p. 030402, Jul 2009.

[26] L. Jin and Z. Song, "Physics Counterpart of the $\mathcal{PT}$ Non-Hermitian Tight-Binding Chain," *Phys. Rev. A*, vol. **81**, p. 032109, Mar 2010.

[27] Y. N. Joglekar and J. L. Barnett, "Origin of maximal symmetry breaking in even $\mathcal{PT}$-symmetric lattices," *Phys. Rev. A*, vol. **84**, p. 024103, Aug 2011.

[28] Y. N. Joglekar, D. Scott, M. Babbey, and A. Saxena, "Robust and fragile $\mathcal{PT}$-symmetric phases in a tight-binding chain," *Phys. Rev. A*, vol. **82**, p. 030103, Sep 2010.

[29] X. G. Wen, "Chiral Luttinger liquid and the edge excitations in the fractional quantum Hall states," *Phys. Rev. B*, vol. **41**, pp. 12838–12844, Jun 1990.

[30] M. C. Zheng, D. N. Christodoulides, R. Fleischmann, and T. Kottos, "$\mathcal{PT}$ optical lattices and universality in beam dynamics," *Phys. Rev. A*, vol. **82**, p. 010103, Jul 2010.

[31] J. Wiersig, "Structure of whispering-gallery modes in optical microdisks perturbed by nanoparticles," *Phys. Rev. A*, vol. **84**, p. 063828, Dec 2011.

[32] W. Heiss and H. Harney, "The Chirality of Exceptional Points," *Eur. Phys. J. D*, vol. **17**, no. 2, pp. 149–151, 2001.

[33] D. D. Scott and Y. N. Joglekar, "Degrees and signatures of broken $\mathcal{PT}$ symmetry in nonuniform lattices," *Phys. Rev. A*, vol. **83**, no. 5, p. 050102, 2011.

[34] T. Schwartz, G. Bartal, S. Fishman, and M. Segev, "Transport and Anderson localization in disordered two-dimensional photonic lattices," *Nature*, vol. **446**, no. 7131, pp. 52–55, 2007.

[35] A. Szameit and S. Nolte, "Discrete optics in femtosecond-laser-written photonic structures," *J. Phys. B: Atomic, Molec. and Opt. Phys.*, vol. **43**, no. 16, p. 163001, 2010.

[36] H. Schomerus, "Universal routes to spontaneous $\mathcal{PT}$-symmetry breaking in non-Hermitian quantum systems," *Phys. Rev. A*, vol. **83**, no. 3, p. 030101, 2011.

[37] Y. N. Joglekar, "Mapping Between Hamiltonians with Attractive and Repulsive Potentials on a Lattice," *Phys. Rev. A*, vol. **82**, no. 4, p. 044101, 2010.

[38] S. Longhi, "Periodic wave packet reconstruction in truncated tight-binding lattices," *Phys. Rev. B*, vol. **82**, p. 041106, Jul 2010.

[39] O. A. Castro-Alvaredo and A. Fring, "A Spin Chain Model with Non-Hermitian Interaction: the Ising Quantum Spin Chain in an Imaginary Field," *J. Phys. A: Math. and Theor.*, vol. **42**, no. 46, p. 465211, 2009.

[40] Y. N. Joglekar, C. Thompson, and G. Vemuri, "Tunable waveguide lattices with nonuniform parity-symmetric tunneling," *Phys. Rev. A*, vol. **83**, no. 6, p. 063817, 2011.

[41] Y. N. Joglekar and A. Saxena, "Robust $\mathcal{PT}$-symmetric chain and properties of its Hermitian counterpart," *Phys. Rev. A*, vol. **83**, no. 5, p. 050101, 2011.

[42] D. D. Scott and Y. N. Joglekar, "$\mathcal{PT}$-symmetry breaking and ubiquitous maximal chirality in a $\mathcal{PT}$-symmetric ring," *Phys. Rev. A*, vol. **85**, no. 6, p. 062105, 2012.

[43] L. Feng, M. Ayache, J. Huang, Y.-L. Xu, M.-H. Lu, Y.-F. Chen, Y. Fainman, and A. Scherer, "Nonreciprocal Light Propagation in a Silicon Photonic Circuit," *Science*, vol. **333**, no. 6043, pp. 729–733, 2011.

[44] H. Vemuri, V. Vavilala, T. Bhamidipati, and Y. N. Joglekar, "Dynamics, disorder effects, and $\mathcal{PT}$-symmetry breaking in waveguide lattices with localized eigenstates," *Phys. Rev. A*, vol. **84**, no. 4, p. 043826, 2011.

[45] M. Znojil, "$\mathcal{PT}$-symmetric square well," *Phys. Lett. A*, vol. **285**, no. 1, pp. 7–10, 2001.

[46] M. Serbyn and M. A. Skvortsov, "Onset of superconductivity in a voltage-biased normal-superconducting-normal microbridge," *Phys. Rev. B*, vol. **87**, no. 2, p. 020501, 2013.

[47] T. Dauxois and M. Peyrard, *Physics of Solitons*. Cambridge, UK: Cambridge University Press, 2006.

APPENDICES

A. APPENDIX

This Matlab code calculates the discrete momentum up to and across the $\mathcal{PT}$ phase boundary on a ring with two on-site $\mathcal{PT}$ impurities.

```
% Code for a ring with two hoppings. The first impurity is at
%position 1 and the other changes position from 2 to N. Note
%that this code is more general than the two code twohoppingsPBC
%where the impurity positions are at m and mbar.

clear;
tic;

N=32; % number of sites.
tR=0.5; % "left chain tunneling".
tL=1.; % "right chain tunneling".
d=32; % second impurity location
H=zeros(N);
for m=1:N-1
        if(m<d)
            H(m,m+1)=-tR;
        else
            H(m,m+1)=-tL;
        end
        H(m+1,m)=H(m,m+1);
end
% define the tunneling between sites 1 and N
H(N,1)=-tL;
H(1,N)=H(N,1);

clean=eig(H);
energyscale=(max(clean)-min(clean))/4;
```

```
timescale=2*pi/energyscale;


w=1;
gammaPT=0.5;
pmax=zeros(16,2);
for gamma=[0:0.1:1.1,0.95,0.99,1.01,1.05]


    % insert impurities
    H(1,1)=1i*gamma*gammaPT;
    H(d,d)=conj(H(1,1));

[V,D]=eig(H);
error=max(imag(diag(D)));

% define time evolution for a given gamma.
T=500; % number of time steps for the time evolution.
psi=zeros(N,T);

momentum=zeros(T,1);

psi0=zeros(N,1);
m0=10; % initial position of the wavepacket.
psi0(m0,1)=1.;

for k=1:T
   t=(k-1)*timescale;
   U=diag(exp(-1i*diag(D)*t));
   psi(:,k)=V*(U/V)*psi0;

   % This routine calculates the average momentum value for a PBC lattice.
   % Note that we also obtain the norm since an initially normalized state
   % may not remain normalized when H is not Hermitian.
   temp=0;
```

```
    norm=0;
    for q=1:N-1
        temp=temp+imag(conj(psi(q+1,k))*psi(q,k));
        norm=norm+abs(psi(q,k))^2;
    end
    temp=temp+imag(conj(psi(1,k))*psi(N,k));
    norm=norm+abs(psi(N,k))^2;
    momentum(k)=-temp/norm;
end


averagemomentum=sum(momentum)/T;
pmax(w,1)=gamma;
pmax(w,2)=averagemomentum;
w=w+1;


end
[y,ix]=sort(pmax(:,1));
     newpmax(:,1)=y;
     newpmax(:,2)=pmax(ix(:),2);
plot(newpmax(:,1),newpmax(:,2))
hold on
toc;
```

B. APPENDIX

This Matlab code calculates the time evolution of a wave packet originally located on a single site on a lattice with tunable hopping.

```
% This code calculates the time evolution across the PT-symmetry
%breaking boundary for a lattice with site-dependent tunneling
%and tunable boundary conditions. It also obtains the Fourier
%transform of the time-evolved wavefunction, and instantenous
%expectation value of the discrete momentum to characterize the
%chiral transport in the ring.

clear;
tic;

N=20; % number of lattice sites. Use power-of-two for FFT.
m=10; % position of the first PT-impurity.
mbar=N+1-m; % position of the other PT-impurity.
lambda=0; % boundary condition scaling parameter

alpha=0; % set the two tunneling parameters.
gamma=1.01;% define and characterize the clean Hamiltonian.
H=zeros(N);
for k=[1:N-1]
    H(k,k+1)=-sqrt(k*(N-k))^alpha;
    H(k+1,k)=H(k,k+1);
end

H(N,1)=-lambda*sqrt(1*(N-1))^alpha;
H(1,N)=H(N,1);
```

```
clean=eig(H);
energyscale=(max(clean)-min(clean))/4;
timescale=1./energyscale;

% put in the impurities.
H(m,m)=1i*gamma;
H(mbar,mbar)=conj(H(m,m));
[V,D]=eig(H);
error=max(imag(diag(D)));
test=abs(det(V));
angle(V(:,1))

bar(abs(V(:,1)))
eigenprob=abs(fft(V));

% define time evolution for a given gamma.
T=3000; % number of time steps for the time evolution.
psi=zeros(N,T);
psikspace=zeros(N,T);
momentum=zeros(T,1);
energy=zeros(T,1);
intensity=zeros(T,2);

psi0=zeros(N,1);
m1=1;
psi0(m1,1)=1.;

for k=1:T
   t=(k-1)*timescale;
   U=diag(exp(-1i*diag(D)*t));
   psi(:,k)=V*(U/V)*psi0;

   % obtain the spatial fourier transform of the wavefunction.
   psikspace(:,k)=fft(psi(:,k));
```

```
    % This routine calculates the average momentum value for a
    %PBC lattice. Note that we also obtain the norm since an
    %initially normalized state may not remain normalized when H
    %is not Hermitian.
    temp=0;
    norm=0;
    for  q=1:N-1
        temp=temp+imag(conj(psi(q+1,k))*psi(q,k));
        norm=norm+abs(psi(q,k))^2;
    end
    temp=temp+imag(conj(psi(1,k))*psi(N,k));
    norm=norm+abs(psi(N,k))^2;
    intensity(k,2)=norm;
    intensity(k,1)=k;
    momentum(k)=-temp/norm;
end

plot(intensity(:,1),intensity(:,2))
meanint=mean(intensity(:,2));
standev=std(intensity(:,2));
averagemomentum=sum(momentum)/T;
probxspace=abs(psi).^2;
probkspace=abs(psikspace).^2;
phasekspace=angle(psikspace);
probp=abs(momentum);
maxpsispace= max(probxspace);
toc;
```

C. APPENDIX

This Matlab code calculates and plots the $\mathcal{PT}$ phase diagram for a sine potential competing with two on-site potentials.

```
clear;
tic;

N=21; % number of sites.
m=1; % position of the first PT-impurity.
mbar=N+1-m; % position of the other PT-impurity.
t0=1; % constant hopping parameter
tolerance=1.e-8;
u=2;

% define and characterize the clean Hamiltonian.
H=zeros(N);
for k=[1:N-1]
    H(k,k+1)=-t0;
    H(k+1,k)=-t0;
end

clean=eig(H); % eigenvalues of the clean Hamiltonian.
bandwidth=max(clean)-min(clean);
escale=bandwidth/4;
increment=0.0001*escale; % governs the increment by which
%gamma is increased.

% Determine critical gamma for on-site potentials when linear
%potential is zero.
nonherm=0;
gammas=0;
```

```
while(nonherm<tolerance)
        gammas=gammas+increment;
        H(m,m)=-1i*gammas;
        H(mbar,mbar)=conj(H(m,m));
        [V,D]=eig(H);
        nonherm=max(imag(diag(D)))/max(real(diag(D)));
end

gammasPT=gammas-increment;

%Determine critical gamma for linear potential when on-site
%potentials are zero.

nonherm=0;
gamma=0;

while(nonherm<tolerance)
        gamma=gamma+increment;
        for k=[1:N]
            H(k,k)=1i*gamma*sin(u*pi*(k-(N+1)/2)/N);
        end
        [V,D]=eig(H);
        nonherm=max(imag(diag(D)))/max(real(diag(D)));
end
gammaPT=gamma-increment;


%Quadrant 1 - Gain-Gain Region - Horizontal Sweep

jmax=40;
increment3=gammaPT/1000;
resultsQ1H=zeros(jmax+1,2);

for j=[0:jmax]
```

```
    H=zeros(N);
    for k=[1:N-1]
        H(k,k+1)=-t0;
        H(k+1,k)=-t0;
    end
    gammaL=0;
    nonherm=0;

    H(m,m)=-1i*j/jmax*gammasPT;
    H(mbar,mbar)=conj(H(m,m));

    while(nonherm<tolerance)
        gammaL=gammaL+increment3;
        for k=[1:N]
            H(k,k)=H(k,k)+1i*increment3*sin(u*pi*(k-(N+1)/2)/N);
        end
        [V,D]=eig(H);
        nonherm=max(imag(diag(D)))/max(real(diag(D)));
    end

    gammaLPT=gammaL-increment3;
    resultsQ1H(j+1,1)=j/jmax;
    resultsQ1H(j+1,2)=gammaLPT/gammaPT;
end
plot(resultsQ1H(:,1),resultsQ1H(:,2),'.')
hold on

%Quadrant 1 - Gain-Gain Region - Vertical Sweep

increment2=gammasPT/1000;
resultsQ1V=zeros(jmax+1,2);

for j=[0:jmax]
    gamma0=0;
    nonherm=0;
```

```
    for k=[1:N]
        H(k,k)=1i*j*(gammaPT/jmax)*sin(u*pi*(k-(N+1)/2)/N);
    end

    while(nonherm<tolerance)
        gamma0=gamma0+increment2;
        H(m,m)=H(m,m)-1i*increment2;
        H(mbar,mbar)=conj(H(m,m));
        [V,D]=eig(H);
        nonherm=max(imag(diag(D)))/max(real(diag(D)));
    end
    gamma0PT=gamma0-increment2;
    resultsQ1V(j+1,1)=gamma0PT/gammasPT;
    resultsQ1V(j+1,2)=(j/jmax);
end
plot(resultsQ1V(:,1),resultsQ1V(:,2),'.')

%Quadrant 2 - Gain-Loss Region - Horizontal Sweep

increment3=gammaPT/1000;
resultsQ2H=zeros(jmax+1,2);

for j=[0:jmax]
    H=zeros(N);
    for k=[1:N-1]
        H(k,k+1)=-t0;
        H(k+1,k)=-t0;
    end
    gammaL=0;
    nonherm=0;

    H(m,m)=1i*j/jmax*gammasPT;
    H(mbar,mbar)=conj(H(m,m));
```

```
    while(nonherm<tolerance)
        gammaL=gammaL+increment3;
        for k=[1:N]
            H(k,k)=H(k,k)+1i*increment3*sin(u*pi*(k-(N+1)/2)/N);
        end
        [V,D]=eig(H);
        nonherm=max(imag(diag(D)))/max(real(diag(D)));
    end

    gammaLPT=gammaL-increment3;
    resultsQ2H(j+1,1)=-j/jmax;
    resultsQ2H(j+1,2)=gammaLPT/gammaPT;
end

plot(resultsQ2H(:,1),resultsQ2H(:,2),'.')

%Quadrant 2 — Gain—Loss Region — Vertical Sweep

increment2=gammasPT/1000;
resultsQ2V=zeros(jmax+1,2);

for j=[0:jmax]
    gammaL=0;
    nonherm=0;
    for k=[1:N]
        H(k,k)=1i*j*gammaPT/jmax*sin(u*pi*(k-(N+1)/2)/N);
    end

    while(nonherm<tolerance)
        gammaL=gammaL-increment2;
        H(m,m)=H(m,m)+1i*increment2;
        H(mbar,mbar)=conj(H(m,m));
        [V,D]=eig(H);
        nonherm=max(imag(diag(D)))/max(real(diag(D)));
    end
```

```
    gammaLPT=gammaL+increment2;
    resultsQ2V(j+1,1)=gammaLPT/gammasPT;
    resultsQ2V(j+1,2)=j/jmax;
end
plot(resultsQ2V(:,1),resultsQ2V(:,2),'.')

%Quadrant 3 - Loss-Loss Region - Horizontal Sweep

increment3=gammaPT/1000;
resultsQ3H=zeros(jmax+1,2);

for j=[0:jmax]
    H=zeros(N);
    for k=[1:N-1]
        H(k,k+1)=-t0;
        H(k+1,k)=-t0;
    end
    gammaL=0;
    nonherm=0;

    H(m,m)=1i*j/jmax*gammasPT;
    H(mbar,mbar)=conj(H(m,m));

    while(nonherm<tolerance)
        gammaL=gammaL-increment3;
        for k=[1:N]
            H(k,k)=H(k,k)-1i*increment3*sin(u*pi*(k-(N+1)/2)/N);
        end
        [V,D]=eig(H);
        nonherm=max(imag(diag(D)))/max(real(diag(D)));
    end

    gammaLPT=gammaL+increment3;
    resultsQ3H(j+1,1)=-j/jmax;
    resultsQ3H(j+1,2)=gammaLPT/gammaPT;
```

```
end

plot(resultsQ3H(:,1),resultsQ3H(:,2),'.')

%Quadrant 3 — Loss—Loss Region — Vertical Sweep

increment2=gammasPT/1000;
resultsQ3V=zeros(jmax+1,2);

for j=[0:jmax]
    gammaL=0;
    nonherm=0;
    for k=[1:N]
        H(k,k)=-1i*j*gammaPT/jmax*sin(u*pi*(k-(N+1)/2)/N);
    end

    while(nonherm<tolerance)
        gammaL=gammaL-increment2;
        H(m,m)=H(m,m)+1i*increment2;
        H(mbar,mbar)=conj(H(m,m));
        [V,D]=eig(H);
        nonherm=max(imag(diag(D)))/max(real(diag(D)));
    end
    gammaLPT=gammaL+increment2;
    resultsQ3V(j+1,1)=gammaLPT/gammasPT;
    resultsQ3V(j+1,2)=-j/jmax;
end
plot(resultsQ3V(:,1),resultsQ3V(:,2),'.')

%Quadrant 4 — Loss—Gain Region — Horizontal Sweep

increment3=gammaPT/1000;
resultsQ4H=zeros(jmax+1,2);

for j=[0:jmax]
```

```
    H=zeros(N);
    for k=[1:N-1]
        H(k,k+1)=-t0;
        H(k+1,k)=H(k,k+1);
    end
    gammaL=0;
    nonherm=0;

    H(m,m)=-1i*j/jmax*gammasPT;
    H(mbar,mbar)=conj(H(m,m));

    while(nonherm<tolerance)
        gammaL=gammaL-increment3;
        for k=[1:N]
            H(k,k)=H(k,k)-1i*increment3*sin(u*pi*(k-(N+1)/2)/N);
        end
        [V,D]=eig(H);
        nonherm=max(imag(diag(D)))/max(real(diag(D)));
    end

    gammaLPT=gammaL+increment3;
    resultsQ4H(j+1,1)=j/jmax;
    resultsQ4H(j+1,2)=gammaLPT/gammaPT;
end
plot(resultsQ4H(:,1),resultsQ4H(:,2),'.')

%Quadrant 4 - Loss-Gain Region - Vertical Sweep

increment2=gammasPT/1000;
resultsQ4V=zeros(jmax+1,2);

for j=[0:jmax]
    gammaL=0;
    nonherm=0;
    for k=[1:N]
```

```
        H(k,k)=-1i*j*gammaPT/jmax*sin(u*pi*(k-(N+1)/2)/N);
    end

    while(nonherm<tolerance)
        gammaL=gammaL+increment2;
        H(m,m)=H(m,m)-1i*increment2;
        H(mbar,mbar)=conj(H(m,m));
        [V,D]=eig(H);
        nonherm=max(imag(diag(D)))/max(real(diag(D)));
    end
    gammaLPT=gammaL+increment2;
    resultsQ4V(j+1,1)=gammaLPT/gammasPT;
    resultsQ4V(j+1,2)=-j/jmax;
end
plot(resultsQ4V(:,1),resultsQ4V(:,2),'.')

toc;
```

VITA

VITA

Derek Douglas Scott

EDUCATION:

- **Doctor of Philosophy**, Physics, Expected: May 2014
  Purdue University, Indianapolis, IN
  DISSERTATION: *An Investigation of Parity and Time-Reversal Symmetry Breaking In Tight-Binding Lattices*
- **Master of Science**, Physics, December 2008
  Indiana University, Bloomington, IN
- **Bachelor of Science (Honors)**, Physics, May 2007
  Purdue University, Indianapolis, IN

TEACHING EXPERIENCE:

- **Recitation Instructor**, **Laboratory Instructor**, **Recitation Mentor**
  Indiana University–Purdue University Indianapolis, Indianapolis, IN 2009 – 2013

PUBLICATIONS:

1. Y. N. Joglekar, **D. D. Scott**, and A. Saxena, "$\mathcal{PT}$-symmetry breaking with divergent potentials: lattice and continuum cases", submitted to *Phys. Rev. A*, currently at arxiv.org/abs/1403.4204 (2014)
2. C. H. Liang, **D. D. Scott**, and Y. N. Joglekar, "$\mathcal{PT}$ restoration via increased loss and gain in the $\mathcal{PT}$-symmetric Aubry-André model", *Phys. Rev. A*, **89**, 030102(R) (2014)

3. Y. N. Joglekar, C. Thompson, **D. D. Scott**, and G. Vemuri, "Optical waveguide arrays: quantum effects and $\mathcal{PT}$ symmetry breaking", Invited Review Article, *Eur. Phys. J. App. Phys.*, **63**, 30001 (2013)
4. **D. D. Scott** and Y. N. Joglekar, "$\mathcal{PT}$ symmetry breaking and maximal chirality in a nonuniform $\mathcal{PT}$-symmetric ring", *J. Phys. A: Math. Theor.*, **45** 444030 (2012)
5. **D. D. Scott** and Y. N. Joglekar, "$\mathcal{PT}$ symmetry breaking and ubiquitous maximal chirality in $\mathcal{PT}$-symmetric ring", *Phys. Rev. A*, **85**, 062105 (2012)
6. **D. D. Scott** and Y. N. Joglekar, "Degrees and signatures of broken $\mathcal{PT}$-symmetry in nonuniform lattices", *Phys. Rev. A*, **83**, 051102(R) (2011)
7. Y. N. Joglekar, **D. D. Scott**, M. Babbey, and A. Saxena, "Robust and fragile $\mathcal{PT}$-symmetric phases in a tight-binding chain", *Phys. Rev. A*, **83**, 030103(R) (2010)

PRESENTATIONS:

- "Modeling Open Quantum Systems with Balanced Loss and Gain Using Non-Hermitian, $\mathcal{PT}$-Symmetric Hamiltonians", *Contributed Talk*, 3rd Anacapa Society Conference, Augusta, Georgia, December 2013
- "Competing $\mathcal{PT}$-Symmetric Potentials and Re-entrant $\mathcal{PT}$-symmetric Phase", *Invited talk*, Third International Conference: Nonlinear Waves Theory and Applications, Beijing, China, June 2013
- "An Introduction to $\mathcal{PT}$-Symmetric Quantum Mechanics with Applications to Lattice Modeling", *Contributed Talk*, 126th Annual Academy Meeting of the Indiana Academy of Science, Indianapolis, IN, March 2011

HONORS AND AWARDS:

- Travel Award, IUPUI School of Science Graduate Student Council 2013
- Outstanding Physics Graduate Student Award 2013
- Graduate Assistance in Areas of National Need Fellowship 2009 – 2012